Monthly Notices
of the
ROYAL ASTRONOMICAL SOCIETY

Mon. Not. R. Astron. Soc. **400,** 743–765 (2009) doi:10.1111/j.1365-2966.2009.14662.x

A blind H I survey in the Canes Venatici region

K. Kovač,[1,2⋆] T. A. Oosterloo[1,3] and J. M. van der Hulst[1]

[1] *Kapteyn Astronomical Institute, University of Groningen, Postbus 800, 9700 AV Groningen, the Netherlands*
[2] *Institute of Astronomy, ETH Zurich, 8093 Zurich, Switzerland*
[3] *Netherlands Foundation for Research in Astronomy, Postbus 2, 7990 AA Dwingeloo, the Netherlands*

Accepted 2009 February 18. Received 2009 February 2; in original form 2008 June 23

ABSTRACT

We have carried out a blind H I survey using the Westerbork Synthesis Radio Telescope to make an inventory of objects with small H I masses (between 10^6 and 10^8 $M_\odot$) and to constrain the low-mass end of the H I mass function. The survey has been conducted in a part of the volume containing the nearby Canes Venatici groups of galaxies. The surveyed region covers an area on the sky of about 86 deg^2 and a range in velocity from about −450 to about 1330 km s^{-1}. We find 70 sources in the survey by applying an automated searching algorithm. Two of the detections have not been catalogued previously, but they can be assigned an optical counterpart, based on visual inspection of the second-generation Digital Sky Survey images. Only one of the H I detections is without an optical counterpart. This object is detected in the vicinity of NGC 4822, and it has been already detected in previous H I studies. 19 of the objects have been detected for the first time in the 21-cm emission line in this survey. The distribution of the H I properties of our detections confirms our ability to find low-mass objects. 86 per cent of the detections have profile widths less than 130 km s^{-1}, and they can be considered dwarf galaxy candidates. The H I fluxes measured imply that this survey goes about 10 times deeper than any previous blind H I survey. The H I mass function and the optical properties of the detected sources will be discussed in future papers.

Key words: methods: observational – catalogues – surveys – radio lines: galaxies.

1 INTRODUCTION

In the currently favoured cosmological models, based on the cold dark matter (CDM) paradigm, structure evolves from the small, primordial, Gaussian fluctuations by gravitational instability. Dark matter haloes grow in a hierarchical manner through multiple merging and accretion of smaller systems (e.g. White & Rees 1978). In the depicted framework, galaxies form by cooling of baryons captured inside the dark matter haloes.

Using the Local Group (LG) as a cosmological probe, a discrepancy between the theory and the optical observations arises, the so-called 'missing satellites problem': the number of observed satellites known in the optical is an order of magnitude smaller than the number of small systems predicted by CDM models (Kauffmann, White & Guiderdoni 1993; Klypin et al. 1999; Moore et al. 1999). Closely related to this problem is a discrepancy between the slopes derived at the faint end of the observed optical luminosity functions (e.g. Blanton et al. 2003) and the H I mass functions (e.g. Zwaan et al. 2005a) on one hand, and the slope of the halo mass functions calculated from large *N*-body CDM simulations (e.g. Jenkins et al. 2001) or from an analytical framework such as the Press–Schechter formalism (Press & Schechter 1974) on the other hand. The faint-end slopes from the observed distributions are much flatter when compared to the corresponding slopes of the theoretically constructed functions.

The absence of a more numerous low-mass galaxy population cannot be straightforwardly understood and points out a lack of our understanding of those systems. The models proposed to solve this discrepancy can be separated into two categories. One type of models is based on the suppression of the formation of small haloes or on their destruction, which can be achieved by modifying the properties of the dark matter. These types of models include allowing finite dark matter particles self-interaction cross-sections (Spergel & Steinhardt 2000), reducing the small-scale power (e.g. Avila-Reese et al. 2001; Bode, Ostriker & Turok 2001; Eke, Navarro & Steinmetz 2001) or changing the shape of the primordial power spectrum (Kamionkowski & Liddle 2000; Zentner & Bullock 2002). Kravtsov, Gnedin & Klypin (2004) suggest that low-mass galaxies form in high-mass haloes that are tidally stripped to form low-mass haloes. The second set of models proposes to suppress the star formation in low-mass haloes. Several plausible baryonic physical processes may cause the depletion of the gas from the haloes, and small haloes will remain dark. Such processes may be quenching of star formation (e.g. Gnedin & Kravtsov 2006), photo-evaporation (see e.g. Quinn, Katz & Efstathiou 1996 and Barkana & Loeb 1999) and/or feedback from supernovae or galactic winds (see e.g. Larson 1974 and Efstathiou 2000). Another possibility to suppress

⋆E-mail: kovac@phys.ethz.ch (KK)

star formation in small haloes is based on stability criteria. During the process of galaxy formation, the angular momentum of gas which settles into the disc is conserved and a number of haloes with small masses may never form stars, or form them in small numbers. According to one of those models, all galaxies with dark matter halo masses below 10^{10} $M_\odot$ will never form stars (e.g. Verde, Oh & Jimenez 2002). Still, baryons will remain inside these small haloes. Recently, Read, Pontzen & Viel (2006) argued that there is a sharp transition of the baryonic content in the smallest haloes. Over the halo mass range 3–10 $\times$ 10^7 $M_\odot$ at $z \sim 10$, the amount of stellar mass drops two orders of magnitude in these systems. Haloes below the limiting mass of $\sim 2 \times 10^7$ $M_\odot$ will be almost devoid of gas and stars. Extrapolating these results to the present redshift (using a combination of arguments based on linear theory and the various literature results), Read et al. (2006) predict the existence of many galaxies with surface brightness about an order or two orders of magnitude fainter than galaxies already detected.

Optical surveys are generally less sensitive to low-luminosity and low surface brightness (LSB) galaxies, which could be underrepresented in such surveys (Disney 1976; Disney & Phillipps 1987). LSB galaxies are found to be rich in neutral gas (Schombert et al. 1992; de Blok, McGaugh & van der Hulst 1996). Given that galaxies with a small amount of stars compared to their H I mass are typically discovered via H I surveys, the blind H I surveys provide an excellent probe to detect galaxies with a small amount of stars. One may detect even a population of completely dark galaxies using an H I survey – under the assumption that dark galaxies contain H I. If one assumes that H I makes up a few per cent of the total mass of a galaxy, dark galaxies would contain H I in the range 10^7–10^8 $M_\odot$ or less. Still one has to be aware that a blind H I survey will miss that part of the population of (dwarf) galaxies without H I (e.g. Geha et al. 2006). Therefore, selection effects of the H I surveys provide limits on the plausible galaxy formation scenarios which a blind H I survey can test.

To complete the story, recent searches for the missing satellites in the local Universe have been conducted by identifying the galaxies in the overdensities with respect to the Galactic foreground in the resolved stellar populations in the nearby optical and infrared surveys. In the photometric data of the Sloan Digital Sky Survey (SDSS; York et al. 2000; Abazajian et al. 2009), 14 new companions of the Galaxy have been discovered, in which nine objects are for sure identified as dwarf spheroidal galaxies (e.g. Willman et al. 2005; Zucker et al. 2006; Belokurov et al. 2008). The galaxies discovered are among the lowest mass and lowest brightest galaxies being known. However, these galaxies have probably been very strongly affected by interactions with the Galaxy (tidal and gaseous, e.g. Grcevich & Putman 2009) and likely remnants of larger galaxies. Their evolution is very complex and highly uncertain. They do not tell the whole story, certainly not about small galaxies in less dense environments.

1.1 Blind H I surveys

In the last three decades, several blind H I surveys have been carried out. The first blind survey in the 21-cm emission line was carried out by Shostak (1977) in driftscan mode, leading to one, not clearly extragalactic, detection. Lo & Sargent (1979) surveyed three nearby groups of galaxies (including CVnI) with the Owens Valley Radio Observatory 40-m telescope, without any discrete H I detection. The higher sensitivity observations of the selected areas of the same groups with the Bonn 100-m telescope resulted in the detection of six H I sources, from which four were previously uncatalogued dwarf galaxies (Lo & Sargent 1979). Krumm & Brosch (1984) surveyed about 7 per cent of the Perseus–Pisces void and about 19 per cent of the Hercules void, with no H I detections. After that, Kerr & Henning (1987, also Henning 1992) conducted a blind H I survey by observing a series of pointings on lines of constant declination. The number of detected objects was 37. Since then, blind H I surveys have yielded sufficient number of detections to describe the results in a statistical manner. The main parameters of the major blind H I surveys are summarized in Table 1, adapted from http://egg.astro.cornell.edu/alfalfa/science.php.

The main conclusion which can be drawn from the (blind) H I surveys carried out up to date is that there is no essential difference between the populations of objects detected in H I emission line surveys and the population of galaxies detected at optical or at infrared wavelengths, except that H I detected galaxies are more gas rich and preferentially of the late morphological types (Zwaan et al.

Table 1. Parameters of major blind H I surveys. The references cited are as follows. 1: Sorar (1994); Zwaan et al. (1997), 2: Kraan-Korteweg et al. (1999), 3: Rosenberg & Schneider (2000), 4: Lang et al. (2003), 5: Braun, Thilker & Walterbos (2003), 6: Meyer et al. (2004), 7: Wong et al. (2006) – the authors do not give the rms estimate, they claim that noise has increased by 31 per cent in the Northern Extension of the HIPASS survey, particularly in the northernmost part (see their fig. 5), 8: Giovanelli et al. (2005). Most of the numbers in the table are based on the Arecibo Legacy Fast ALFA (ALFALFA) survey webpage (http://egg.astro.cornell.edu/alfalfa/science.php). The surveys are ordered by the year of publishing results. ALFALFA is the last entered survey, as it is still ongoing.

Survey	Area (deg^2)	Beam size (arcmin)	Velocity range (km s^{-1})	Velocity resolution[a] (km s^{-1})	Detections (number)	($\min M_{\rm H\,I}$)[b] ($10^6 \times M_\odot$)	Telescope	Ref
AHISS	65	3.3	−700–7400	16	65	1.9	305-m Arecibo	1
Nançay CVn	800	4 × 20	−350–2350	10	33	20	Nançay	2
ADBS	430	3.3	−650–7980	34	265	9.9	305-m Arecibo	3
HIJASS	1115	12	−1000–4500 7500–10 000	18	222	36	76-m Jodrell Bank	4
WSRT WFS	1800	49	−1000–6500	17	155	49	WSRT	5
HIPASS	21346	15.5	300–12 700	18	4315	36	64-m Parkes	6
HIPASS Northern extension	7997	15.5	300–12700	18	1002	x	64-m Parkes	7
ALFALFA	7000	3.5	−2000–18 000	11	(>25 000)	4.4	305-m Arecibo (in progress)	8

[a]The given velocity resolution is after the Hanning smoothing.
[b]Minimum detectable masses min $M_{\rm H\,I}$ are calculated at 10 Mpc for 5σ detections with velocity width 30 km s^{-1}.

2005a). A new population of isolated, self-gravitating H I clouds or dark galaxies has not been revealed; neither has a large population of galaxies with low optical surface brightness, which would have gone undetected in optical surveys (e.g. Zwaan et al. 2005a). The distribution of H I selected objects follows the large-scale structures defined by optically selected galaxies (Koribalski et al. 2004; Zwaan et al. 2005b), but these objects tend to populate regions of lower density (Ryan-Weber 2006; Basilakos et al. 2007). However, to be able to get a more definitive answer to the question whether an additional number of gas-rich low-luminosity and LSB galaxies and/or a population of gas-rich dark galaxies, missed in the optical surveys, exists, it is necessary for H I surveys to reach lower H I mass limits.

Even though the minimum H I masses which can be detected in the blind H I surveys are a few times $\sim 10^6$ M$_\odot$ (see Table 1), only a small number of galaxies have been detected with such small H I masses, particularly beyond the LG. Such detections include ESO 384-016 with the H I mass 6×10^6 M$_\odot$ (Beaulieu et al. 2006), four galaxies in Sculptor with the H I mass 2–9 $\times 10^5$ (Bouchard et al. 2005) and four galaxies in Centaurus with the H I masses below 10^7 M$_\odot$ (Minchin et al. 2003). All of these detections have optical counterparts. On the other hand, there is a population of high-velocity clouds (HVCs; e.g. Wakker & van Woerden 1991; Braun & Burton 2000; de Heij, Braun & Burton 2002) discovered only in the 21-cm line (no optical counterparts have yet been found). These objects are distributed all over the sky, either as extended complexes or in the form of compact, isolated clouds (these are referred to as compact HVCs, or CHVCs). The nature of the (C)HVCs is a matter of debate, despite nearly four decades of study. The main reason for this is the difficulty in estimating distances to the (C)HVCs. However, there are a number of HVCs with well-constrained distance brackets via observations of absorption lines towards stars in the Galactic halo [such as Complex A (Wakker et al. 1996), Complex C (Wakker et al. 2007; Thom et al. 2008), the Cohen Stream (Wakker et al. 2008), Complex GCP (or Smith Cloud; Wakker et al. 2008) and Complex WB (Thom et al. 2006)]. The measurements place these complexes within about 10 kpc of the Sun, putting some constraints on the nature of the HVC complexes. There is little doubt that the Magellanic Stream, a $100^\circ \times 10^\circ$ filament of gas extending within the Galactic halo, is produced by interactions between the Milky Way and companions, as a result of either tidal disruption or ram pressure stripping, or both (e.g. Putman et al. 1998, 2003; Putman & Gibson 1999). Some of the extended HVCs can be explained as the products of Galactic fountains (Shapiro & Field 1976; Bregman 1980, 1996). Blitz et al. (1999) proposed a dynamical model in which the HVCs can be explained as the gaseous counterparts of the primordial low-mass haloes predicted by ΛCDM structure formation scenarios. This appeared as a very attractive way to resolve the discrepancy on the number of low-mass systems discussed above. The origin of CHVCs is more uncertain. One of the hypotheses that has received recent attention is that the CHVCs are of primordial origin, residing at typical distances of up to 1 Mpc from the Milky Way (Oort 1966, 1970; Kerr & Sullivan 1969; Verschuur 1969). The recent observations (Zwaan 2000; Pisano et al. 2004; Westmeier, Brüns & Kerp 2005; Pisano et al. 2007) and simulations (Sternberg, McKee & Wolfire 2002; Kravtsov, Gnedin & Klypin 2004) do not confirm the existence of a circumgalactic population of CHVCs. The results by Westmeier et al. (2005) suggest an upper limit of about 60 kpc for the distance of CHVCs from their host galaxies. This distance would lead to a limiting H I mass for CHVCs of 6×10^4 M$_\odot$. Similarly, Pisano et al. (2007) infer a maximum distance of 90 kpc for the CHVCs, with average H I mass smaller than or equal to 4×10^5 M$_\odot$. So far, there is no observational evidence for a population of H I clouds more massive than 10^7 M$_\odot$ that are not directly associated with a galaxy (Sancisi et al. 2008).

Recently, there was a lot of debate on the nature of a few H I detections without an obvious optical counterpart – whether they are dark galaxies or not (e.g. VIRGOHI 21 reported by Davies et al. 2004 and confirmed by Minchin et al. 2005 and the HVC Complex H discussed by Lockman 2003 and Simon et al. 2006). Kent et al. (2007) report the discovery of the eight H I features lacking a stellar counterpart (four of them already known, including the VIRGOHI 21 object) detected as a part of the ALFALFA survey (Giovanelli et al. 2005). All of these eight H I features are within the region of Virgo cluster, and if at the Virgo distance their H I masses span a range between 1.9×10^7 and 1.1×10^9 M$_\odot$ (Kent et al. 2007). The HVC Complex H is at the distance d of 27 ± 9 kpc from the Sun (Lockman 2003) and with the H I mass of $\sim 2.7 \times 10^4 d^2$ M$_\odot$ (Wakker et al. 1998). So far, there is no confirmation that these detections are gravitationally bound objects, residing within a dark matter halo. Based on the deeper ALFALFA data (Haynes, Giovanelli & Kent 2007), as well as on modelling of the Westerbork Synthesis Radio Telescope (WSRT) data (Duc & Bournaud 2008), VIRGOHI 21 has been reported to be a tidal feature of NGC 4254 with the H I mass of 3×10^7 M$_\odot$ (Minchin et al. 2007).

The existing H I surveys are incomplete in the range of H I masses (10^7–10^8 M$_\odot$ and below) which would correspond to the majority of galaxies predicted to exist with little or no stars. The few detected objects known in this mass range are all associated with nearby galaxies detected in the optical and do not represent the predicted class of small galaxies with gas but no stars. To be able to address the question of whether such objects exist and in which numbers, a deeper blind H I survey is needed, in which galaxies with H I masses below 10^8 M$_\odot$ are a significant fraction of all detections.

We carried out a new blind H I survey designed to be extremely sensitive to objects with H I masses below 10^8 M$_\odot$. The inventory of these objects allows us to derive the number density of the low H I mass objects and to constrain the slope of the low-mass end of the H I mass function about a decade lower than any previous study. We leave the estimation of the H I masses of the detections and the H I mass function for a follow-up paper (see also Kovač 2007). In this work, we present the survey and the detections. This paper has been organized as follows. In Section 2, we present the observational setup and data reduction. In Section 3, we describe the method used to search for the signal and the H I parametrization. We present the uncertainties of the measured parameters and the completeness of the survey in Section 4, and discuss the various H I properties of the observed detections in Section 5. In Section 6, we give a final summary. At the end, in Appendix A, we provide an atlas of the figures emphasizing the various properties of the detections. (The full appendix is available in the online version of the article; see Supporting Information.) Throughout the paper, we express the coordinates of the objects in the J2000 system.

2 DESCRIPTION OF THE SURVEY

Due to technical limitations of the current cm-wave radio telescopes, the volumes probed by H I surveys are much smaller than volumes probed by optical and infrared surveys. Moreover, to date these surveys have been sensitive to objects with small H I masses (below 10^8 M$_\odot$) only up to distances of a few (tens) Mpc (see Table 1). Therefore, to be able to make an inventory of objects with small

H I masses in a reasonable amount of telescope time, only a nearby volume can be targeted for such search.

2.1 The selected volume

We have selected a part of the nearby volume containing galaxies residing in the Canes Venatici (CVn) groups (or clouds) to carry out a blind H I survey. The CVn groups of galaxies are concentrated in a small area in the constellation of the same name (Karachentsev et al. 2003; constellation limits are $11^{\rm h}30^{\rm m} < \alpha < 13^{\rm h}40^{\rm m}$ and $25^\circ < \delta < 55^\circ$), known to host a population of small galaxies. Together with the LG and the loose group in Sculptor, the CVn galaxies extend along the line of sight up to a distance corresponding to $cz \approx 1200\,{\rm km\,s^{-1}}$ (or to about 17 Mpc assuming $H_0 = 70\,{\rm km\,s^{-1}\,Mpc^{-1}}$ and Hubble flow). The study of the velocity flow in the nearby volume of the CVn groups by Karachentsev et al. (2003) reveals that galaxies in this region closely obey a Hubble flow. The prospect of using the Hubble flow to estimate distances to the objects even for such small recession velocities makes the CVn region an excellent target for the H I observations.

Two concentrations can be distinguished in the CVn groups (Tully & Fisher 1987). The redshift distribution of galaxies shows a peak at $V_{\rm LG} = 200$–$350\,{\rm km\,s^{-1}}$, which corresponds to the galaxies in the CVnI cloud. Another peak is seen in the range of $V_{\rm LG} = 500$–$650\,{\rm km\,s^{-1}}$ and may correspond to a more distant cloud CVnII aligned along the Supergalactic equator. The better-studied CVnI cloud is populated mostly by late-type galaxies of low luminosity, in contrast to the groups in the CVnI neighbourhood: the M81, Centaurus and Sculptor groups. The apparent overdensity of the number of galaxies seen in the CVn direction exceeds $\delta N/N \sim 7$ (Karachentsev et al. 2003).

We will refer to the volume covered by our survey as the CVn region from now on. The exact limits of the observed region are given in the following section.

2.2 WSRT observations

During 2001, 2002 and 2004, observations comprising a total of approximately 60×12 h have been performed for this survey using the WSRT. The WSRT is an aperture synthesis interferometer with 14 antennas arranged in a linear array on a 2.7 km east–west (EW) line. 10 of the telescopes are fixed, while four antennas are movable on two rail tracks. The antennas are equatorially mounted 25 m dishes. In a single 12-h time slot, 24 fields were observed in mosaic mode. These fields are on an EW line and are separated by 15 arcmin in right ascension. On different days, similar strips of constant declination were observed. The separation in declination between strips is 15 arcmin. Given that the full width at half-maximum (FWHM) of the WSRT primary beam is 34 arcmin, we obtained a nearly uniform sensitivity over the whole observed area with the 15 arcmin sampling used. Each of the 24 fields in one strip of constant declination was observed for 100 s before moving to the next pointing, which gives 18 different uv scans per field per 12 h period. Using interlaced sampling on different days (the pointings observed first during two consecutive nights of observations are shifted by 15 arcmin in right ascension), the uv coverage improved to 36 uv scans per observed pointing. The effective integration time per pointing was 80.1 min (taking the slew time into account). The shortest spacing of the array used for the observation was 36 m. All structures larger than 20 arcmin will be filtered out completely. Structures smaller than 10 arcmin should, however, be recovered quite well.

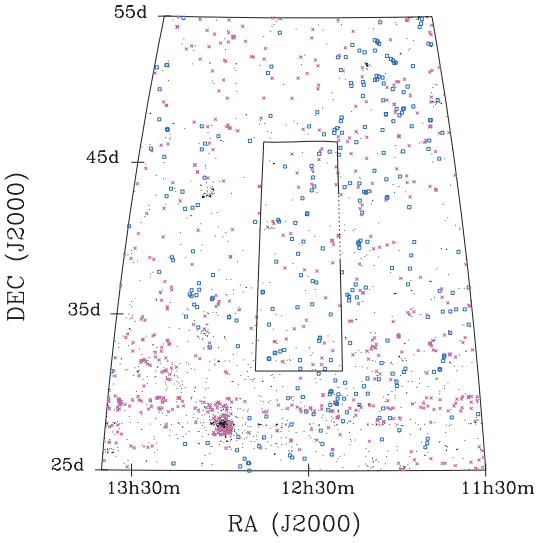

Figure 1. Surface distribution of galaxies in the CVn region. Every point in the plot corresponds to one detection in the CfA redshift survey catalogue (Huchra et al. 1999). From these, galaxies with the recession velocities $V_{\rm LG} \leq 2000\,{\rm km\,s^{-1}}$ are presented with squares. Detections for which redshift measurement has not been provided are indicated by crosses. The area covered by the WSRT CVn survey has been marked with the combination of a continuous and a dotted line. The dotted line corresponds to the range in declinations for which two pointings per strip of constant declination have not been observed.

The first 9×12 h, performed in 2001, were observations with one 10-MHz wide band with 128 channels covering the velocity range of approximately -450 to $1450\,{\rm km\,s^{-1}}$. The rest of the observations were carried out in two bands. Then, we used one band of 20 MHz width with 512 channels covering the velocity range from -750 to about $3250\,{\rm km\,s^{-1}}$. The second band used was 20 MHz wide with 512 channels covering roughly the interval from 3000 to $7000\,{\rm km\,s^{-1}}$. Only data with approximately $-450 < cz < 1330\,{\rm km\,s^{-1}}$ were used in the further data reduction and analysis process.

All the pointings for the survey were located within the area on the sky with limits $12^{\rm h}19^{\rm m}55\overset{\rm s}{.}2 \leq \alpha \leq 12^{\rm h}47^{\rm m}2\overset{\rm s}{.}4$ for $\delta = 31^\circ33'\,00''$ and $12^{\rm h}16^{\rm m}42\overset{\rm s}{.}9 \leq \alpha \leq 12^{\rm h}50^{\rm m}3\overset{\rm s}{.}0$ for $\delta = 46^\circ18'00''$. Due to a human error in the observational setup, two of the first four pointings with the smallest right ascension have not been observed for strips with declination between $38^0\,48'\,00''$ and $42^\circ48'\,00''$. Therefore, the observed area on the sky is approximately 86 deg^2 (instead of the originally planned 90 deg^2). Fig. 1 shows the projected distribution of galaxies in the CVn region [constellation limits taken from Karachentsev et al. (2003) are given above]. Detections are taken from the Center for Astrophysics (CfA) redshift survey catalogue (Huchra, Vogeley & Geller 1999).

2.3 Data reduction

In total, 1372 (useful) pointings were observed for this survey. Scripts were developed to automate the processing for this large number of pointings. The scripts were based on MIRIAD program (Sault, Teuben & Wright 1995) and programs written by two of us (TAO and KK). The data reduction process applied is described below.

The uv data of each pointing were cross-calibrated and Hanning smoothed. The few first and last channels in the observed band

were excluded because of their higher noise. The data were visually inspected, and obviously bad data were flagged. To be able to see the H I emission in the observed data, the continuum had to be subtracted. The continuum *uv* data were created to first approximation by fitting a polynomial of second order to all available channels for each pointing, excluding the obvious line emission. After summing the continuum emission observed over the whole band into one plane, the data were Fourier transformed into (α, δ) continuum images using standard MIRIAD programs. The final continuum image was created in an iterative process of cleaning and self-calibration of the continuum data. The line *uv* data were obtained by copying the calibration coefficients and subtracting the modelled continuum emission from the observed data in the *uv* domain.

The line *uv* data were processed into (α, δ, V) line datacubes using the MIRIAD program INVERT. The mosaicking mode of the observations produced data sampled very sparse in the *uv* plane. In order to suppress large, shallow wings of the synthesized beam, a special weighting was applied to the *uv* points. This weighting corresponds to natural weighting multiplied by radius in the *uv* plane. The data were smoothed spatially by multiplying the *uv* data with a Gaussian corresponding to a FWHM of 30 arcsec. From the first 9×12 h of observations, 216 line datacubes each consisting of 115 channels (i.e. [α, δ] images) were obtained. The rest of the data were processed into 1156 line datacubes with 125 channels. Additional continuum subtraction was applied to all pointings by fitting the continuum with a polynomial of the first order to the line datacubes excluding line emission, and subsequently subtracting it from them. The velocity spacing in the line datacubes produced is $\sim$16.5 km s^{-1} and the velocity resolution after the Hanning smoothing is $\sim$33 km s^{-1}. The size of the image in each of the channels is 512×512 pixels^2, with a pixel size of 8×8 arcsec^2. The typical spatial resolution of the datacubes produced is $\sim 30 \times 60$ arcsec^2.

A known problem for detecting radio emission is man-made and natural interference. No good automated method exists for removing interference from the data, especially not from data observed in mosaicking method. In these kinds of observations, marking the data as bad outside an interval of data values observed for an individual source (e.g. 'sigma-clipping') will not necessarily remove the data affected by interference. The scatter seen in the data can be caused both by the interference and by the observed source itself, because the *uv* properties of a source can significantly change between the two consequent observations in the mosaic mode of that specific pointing. Therefore, all 1372 line datacubes were visually inspected. Datacubes are composed of 36 different *XX*, *YY* scans, and if interference occurred it was easily recognizable in the image domain, where the interference appeared as a strong narrow stripe. An example of the appearance of interference in the datacubes is presented in the three upper panels in Fig. 2. Using the MIRIAD task CGCURS, stripes induced by the interference were marked and removed by flagging the *uv* scan during which the interference occurred.

As a result of the sparse sampling in the *uv* plane, the sidelobe levels and grating rings around the strong H I sources preclude detecting faint H I emission. Channels with H I emission were CLEANed and RESTOREd with a Gaussian beam with a similar FWHM as the synthesized beam corresponding to the pointing. In the three middle panels in Fig. 2, we show an example of grating rings produced around an H I source.

To exploit the observing strategy with overlapping pointings, line datacubes corresponding to the pointings with separation less or equal to 22 arcmin were combined into one datacube. Smaller datacubes of size $150 \times 150 \times 115$ or $150 \times 150 \times 125$ pixel^3 in $\alpha \times \delta \times V$ directions, respectively, were cut out of the central part of each combined datacube, where the size of the third dimension depends on the observations. The *uv* continuum subtraction worked well, leaving only minor residual effects in the image datacubes. These residual continuum features were removed using a simple linear baseline fit to the spectra in the datacube excluding the channels with H I emission. The small, combined line datacubes have been used for all of the further data analysis. In the following text, they will be referred to as the full resolution datacubes. An example of the full resolution datacube is presented in the three lowest panels in Fig. 2.

For each of the combined datacubes, the synthesized beam of the central datacube used in the combining process was chosen as the beam of that datacube. Theoretically, all the *uv* data observed in overlapping pointings could be used jointly to build a single large data cube, instead of applying the whole data reduction process on the individual pointings and then combining the cleaned and interference-free line datacubes from the individual pointings. In practice, the first method would need much more computer time and computer memory, and at the moment it is not affordable for such a large data set as ours.

3 H I DETECTIONS

3.1 Searching for detections

One of the most important aspects of analysing the observations is to define what constitutes a detection. In surveys, regardless of the observed wavelength, the common way is to consider a detection to be a real object if the measured flux, or part of it, of that particular object exceeds the noise by a certain factor (e.g. Wall & Jenkins 2003).

The line datacubes, produced as described in the previous section, were smoothed both in the spatial and in the velocity domain in order to improve the detectability of extended objects with small signal-to-noise ratios. The datacubes were convolved with Gaussians with FWHMs such that the final spatial resolution of the produced smoothed datacubes was 1.5 and 2.0 times the original spatial resolution. In the velocity domain, cubes were Hanning smoothed by performing a weighted average of the fluxes over five and seven neighbouring channels. Smoothing in the spatial and velocity domain was done separately.

To get a good insight in the statistical properties of the data, the mean and the rms values of datacubes were estimated for all of the 1372 line datacubes produced at the five different resolutions (the full resolution, two smoothed in the spatial domain and two smoothed in the velocity domain). The mean and the rms values of the individual datacubes were estimated from the pixels with absolute flux values below five times the preliminary rms value of the datacube. The preliminary rms was estimated using all of the pixels in the datacube. The binned distribution of the final rms values is presented in Fig. 3, while the mean and the standard deviation of the measured rms values are presented in Table 2. For reference, we include in Table 2 the typical spatial and velocity resolution of the specific types of datacubes, as well as the limiting column density to detect an object with a profile width equal to the velocity resolution (third column in Table 2) at the 5σ (five times the value in the fourth column in Table 2) level. The mean noise value in the line datacubes with the full resolution is 0.86 mJy beam^{-1}. For an object with a velocity width of 30 km s^{-1} and an H I mass of 10^6 M$_\odot$, this noise limit would imply a maximum distance of 5.7 Mpc at which this object could be placed and still be detected in the survey at

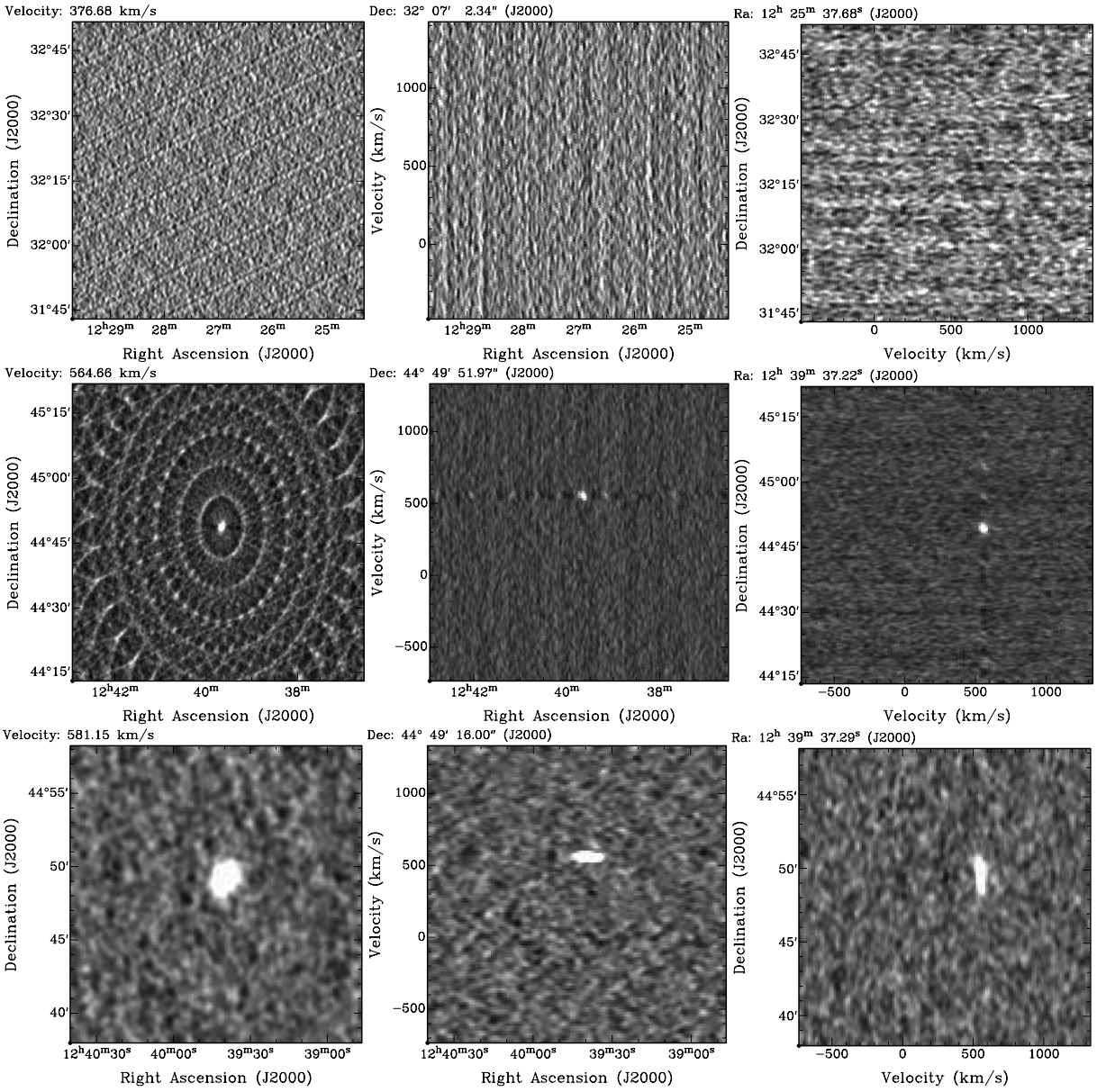

Figure 2. Examples of the various features in the line datacubes. The panels in the vertical direction are made by extracting one slice from the line datacubes in $\alpha - \delta$, $\alpha - V$ and $\delta - V$ planes, going from left- to right-hand side, respectively. Three uppermost panels show the appearance of the interference in the datacubes. The middle panels illustrate the grating rings formed around an H I source. The lowest panels show cuts through a final line datacube produced by combining nine of the line datacubes, created from the data observed for one pointing, and by cutting the central part of the combined datacube.

Table 2. Statistics of the 1372 line datacubes. The first row corresponds to the statistics of the full resolution datacubes. Statistics of the datacubes Gaussian smoothed in the spatial resolution by a factor of 1.5 and 2 is given in the second and third rows, respectively. Statistics of the datacubes Hanning smoothed over five and seven neighbouring velocity channels are presented in the fourth and fifth rows, respectively. See text for description of the columns.

	Resolution		rms		$N_{\rm H\,I}$
Datacube type	Spatial (arcsec^2)	Velocity (km s^{-1})	Mean (mJy beam^{-1})	rms (mJy beam^{-1})	(10^{20} × atoms cm^{-2})
1.0	30 × 60	33	0.86	0.30	0.87
G1.5	45 × 90	33	1.33	3.01	0.60
G2.0	60 × 120	33	1.64	3.98	0.42
H5	30 × 60	82.5	0.67	0.28	1.70
H7	30 × 60	99	0.62	0.28	1.88

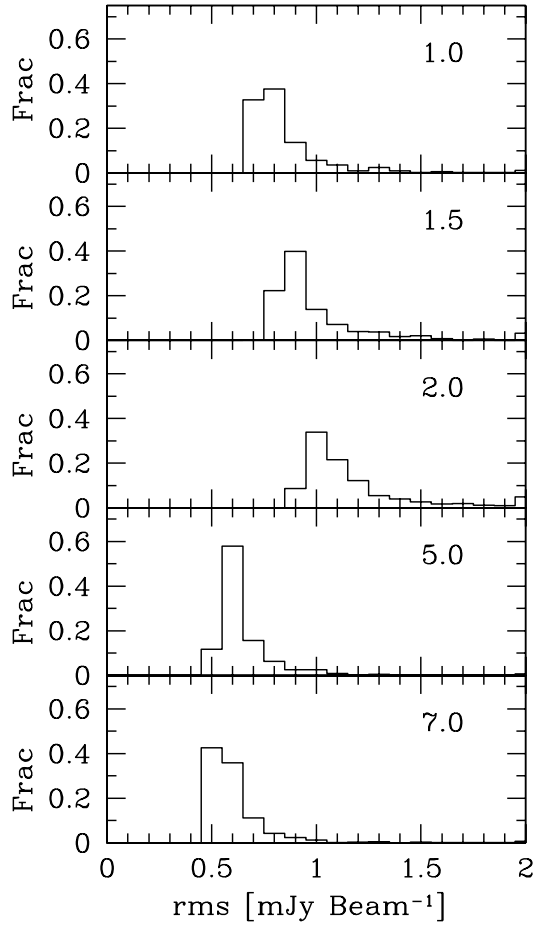

Figure 3. Statistics of the line datacubes. The panels show the histogram distributions of rms values measured for 1372 datacubes produced. In the first row, results from the measurements in the datacubes with full resolution are presented. The second and the third rows contain the results for the datacubes smoothed in the spatial domain to the resolution 1.5 and two times the original resolution, respectively. The fourth and the fifth rows present the statistics for the datacubes Hanning smoothed in the velocity domain averaging fluxes over five and seven neighbouring channels, respectively.

the 5σ level. In the same type of datacubes, the limiting column density to detect an object with a velocity width of 30 km s^{-1} at the 5σ level is 7.9×10^{19} atoms cm^{-2}. This is only a crude estimate of the detection limit of the survey. A more precise estimate of the detection limit, based on the Monte Carlo simulations, will be presented in Section 4.2.

The distribution of the observed pointings in this survey was designed in such a way that the noise in the combined datacubes is almost uniformly distributed. Still, the noise in some of the datacubes shows a gradient in the spatial domain along the declination axis. This is due to the fact that the final datacube is composed from observations typically collected during three different nights. The noise gradient reflects the difference in quality of the data collected during each single 12-h period of observations caused by, for instance, the loss of one of the 14 telescopes and the difference in the data flagging.

To overcome this problem, the noise in each pixel of the datacubes was modelled by averaging the standard deviations independently estimated in the spatial and velocity projections in the following way. First, the standard deviation of the flux values in the spectra at the position of every pixel in the spatial domain along the velocity was calculated. The standard deviation of the fluxes was calculated also for each of the channels in the datacube. For these calculations, pixels in the channels around zero velocity, where the Galactic emission can be very strong, were excluded. In the second iteration, in addition to the pixels in the region of Galactic emission, pixels with flux values larger or equal to five times noise from the first iteration were excluded also from the calculations. The 'characteristic noise' of a pixel in a datacube was defined as the average value of the two standard deviations calculated in the second iteration for the plane and for the spectrum which both contained that pixel. This value will be referred to in the text as the noise (σ). The velocities with Galactic emission are in the range from approximately -50 to 80 km s^{-1} and from approximately -60 to 85 km s^{-1} for the datacubes produced from the pointings observed during the first 9×12 h and during the remaining observations, respectively.

The next step was to inspect the line datacubes in order to detect the presence of H I emission. All line datacubes were searched for pixels with an absolute flux value above a given limit expressed in multiples of the noise in each pixel. A procedure was developed to automate the process of searching for signal in the datacubes.

First, the procedure was used to find all pixels with absolute flux values above 5σ in the datacubes of the five different resolutions. For a comparison of the detections, the search was also performed to detect pixels with absolute flux values above 4σ for the line datacubes at the full resolution. The number of connected pixels with flux values above the given threshold (positive pixels in the remaining text) or below -1 times the given threshold (negative pixels) was counted. Pixels were classified as connected if they had at least one neighbouring pixel which passed the same searching criteria either in the spatial or in the velocity domain. Negative velocity regions were searched for galaxies, but the velocity range with Galactic emission (the same velocity intervals as in the noise calculations) was excluded from this search. The results of the process of the search for the regions of connected pixels are presented in Fig. 4. The upper parts of all panels show the distribution of counts of the regions of connected pixels with positive flux values above the given threshold and negative flux values below -1 times the given threshold. The lower parts of all panels present the difference between the number counts of the regions of connected pixels with positive and negative flux values of a specific size over a range of sizes, where the size is expressed in pixels.

The thresholds to consider a detection as a real object were determined from the distributions of the number of connected positive and negative pixels for each of the six explored cases. The criteria were based on the expectation that the noise is distributed symmetrically. Detections were considered real objects if the number of connected positive pixels was larger than the largest number of connected negative pixels, which obviously corresponds to noise. For the datacubes with full resolution, a detection then is a real object if the number of connected pixels with flux values larger than or equal to 5σ is larger than or equal to 10 pixels and the number of connected pixels with flux values larger than or equal to 4σ is larger than or equal to 22 pixels. The typical beam size is approximately 32 pixels for the datacubes with full resolution. For the datacubes smoothed in the spatial resolution by a factor of 1.5 and 2, a detection would be considered real if it contains larger than or equal to 15 and larger than or equal to 25 connected pixels with flux values larger than or equal to 5σ, respectively. For the datacubes Hanning smoothed in velocity over five and seven channels, the number of connected pixels with flux values larger than or equal to 5σ had to be larger than or equal to 12. From the distributions of all connected pixels with flux values in a certain interval, especially

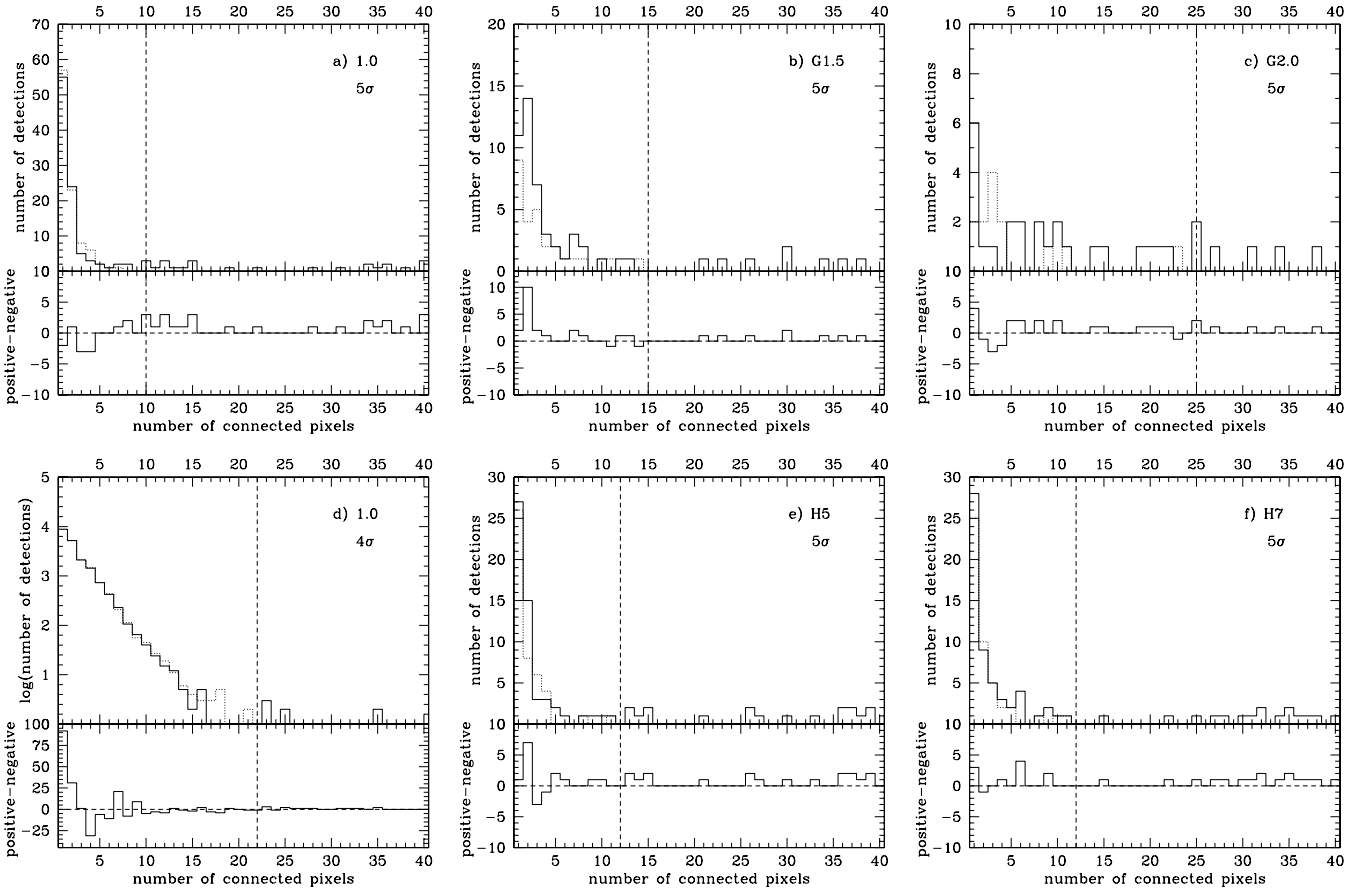

Figure 4. Distributions of counts of connected pixels with a certain positive and negative flux value revealed in the searching process. The upper parts of all panels show the distribution of counts of the regions of connected pixels with positive flux values above the given threshold (full line histograms) and negative flux values below −1 times the given threshold (dotted line histograms). The threshold is 5σ for the three upper (a, b, c) and the last two lower (e and f) panels and 4σ for panel (d). The vertical dashed line marks the position of the minimum number of connected pixels for a detection to be considered a real object. The lower parts of all panels present the difference between the number counts of the regions of connected pixels with positive and negative flux values of a specific size over a range of sizes, where the size is expressed in pixels. The panels (a) and (d) show the results of the searching process on datacubes with the full resolution. Panels (b) and (c) show the results of the searching process done on datacubes spatially smoothed with the Gaussians to the resolution 1.5 (panel b) and two (panel c) times the original spatial resolution. Results for the datacubes Hanning smoothed averaging over five neighbouring channels are presented in panel (e) and for the datacubes Hanning smoothed averaging over seven neighbouring channels are presented in panel (f).

from the differences between the numbers of positive and negative connected pixels with the same number of pixels (Fig. 4), it is obvious that there is no hidden distinct population of H I sources with flux values at the sub-noise levels. Such a population of missed objects would have been easily recognizable as a systematic offset of the difference between the positive and negative pixels with the same number of connected pixels towards positive values.

Applying the determined criteria, a unique catalogue of H I detections was created by the union of the six catalogues obtained by applying the specific searching criteria on the line datacubes of different type. In total, our search criteria reveal 70 H I detections which are considered real. All 70 detections were catalogued already in the datacubes with full resolution. No additional detection passed the 'real object' criteria in the datacubes that were smoothed either in the spatial or in the velocity domain. There are no detections with lower column densities than the limiting column density which has already been achieved in the line datacubes at the full resolution.

There were four regions detected where the H I emission was very extended and the objects detected in these regions were of extremely irregular shape. For these cases, the final decision what is an object was made by eye, after consulting previous observations available from the literature. These H I objects will be termed extended from here on. The extended objects are the objects with the WSRT-CVn IDs ranging from 63 and 68 including (with two objects with the WSRT-CVn ID 67: 67A and 67B). More details on these and the rest of the objects will be given in the following text.

3.2 H I parametrization

The H I parametrization of the detected objects was carried out combining programs developed for this survey and standard MIRIAD programs. The cubes with full resolution in the spatial and velocity domains were used to determine the parameters of the H I detections.

The next task after the detection of the objects was to determine the total flux of the object. Due to the uncertainty of the process, we have done this in two ways and taken the average of the two measurements as the total flux estimate.

The first method was to select the pixels which belong to an object (i.e. to mask all pixels with the signal). This was done in two steps. The first step was developed in order to recover the total flux of an object, and the second step was developed to recover the

shape of an object. Starting from the pixel of the detection with the maximum flux value, the object was enlarged considering that all connected pixels with flux values larger than or equal to 3.5σ belong to the object, using our definition of σ. The 3.5σ limit was obtained as the optimal limiting flux value after testing various assumed limits to recover the total flux of an object in the INVERTED datacubes. For this test, we used the clean components of various objects inserted into the line datacubes, convolved with a cleaned beam of the datacube of the consideration previous to the insertion. The second step consisted of changing the shape of the masked pixels in each of the planes where the object was detected with significance above 3.5σ, to account for the fact that the detections in line datacubes are convolved with the beam of some finite size (which defines the spatial resolution element). First, to remove the detected pixels which are most probably only the noise, pixels with more than three neighbouring pixels which do not belong to the object (their flux values are smaller than 3.5σ) were deleted. After that, remaining pixels in the mask with at least one neighbouring pixel which does not belong to the object were marked as the border pixels. For each of the border pixels an area of a beam size centred on the border pixel was inspected. All pixels with positive flux values inside the beam area studied were added to the detection. The total integrated flux ($S_{\rm int,c}$) of the detections was obtained by summing the flux in pixels determined to belong to the object in all channels and dividing this value by the beam area. The spatially integrated peak flux is simply the maximum value of the fluxes integrated in the individual channels (maximum in the spectrum, $S_{\rm peak,c}$). From now on, we will use the term integrated flux instead of the total integrated flux and the term integrated peak flux instead of the spatially integrated peak flux.

The size of the detected objects, which were not classified as extended objects, was estimated using the MIRIAD task IMFIT. A two-dimensional Gaussian was fitted to the H I map, created by integrating the flux over the velocity channels contained in the masked pixels. When possible, we estimated the size of an object from the size of an ellipse fitted to a column density isophote of 1.25×10^{20} atoms cm^{-2}. This isophotal level corresponds to a value of $1\,{\rm M}_{\odot}\,{\rm pc}^{-2}$. For the small objects (WSRT-CVn 7, 10, 11, 12, 15, 19, 22, 25, 30, 31, 42, 43, 47 and 61), we used the FWHMs of the fitted Gaussian along the major and minor axes as a *rough* indicator of the angular size of an object. The FWHMs along major and minor axes and the positional angles obtained were deconvolved with the beam. The exceptions are detections with the WSRT-CVn IDs 7 and 47, which are too small to be deconvolved. For these two detections, we present only the values of the FWHMs of a two-dimensional Gaussian convolved with a beam instead of their size. The last parameters will be used only as an indication of the inclination of these two objects. For the objects without a known counterpart in the literature, we use the position of the peak of the fitted Gaussian as the position of that particular object (the cross-correlation with literature detections is described in Section 5.1). Most of our detections are very small and the estimated H I sizes are very uncertain (see Table 4, later for the objects with an estimated size comparable to or smaller than the beam size we use a '<' sign to indicate that these sizes are probably just upper limits). However, they are useful for a comparison with the sizes estimated from the optical measurements. We do not measure H I sizes of the extended objects, as the noise distribution in the datacubes of these objects is much more inhomogeneous, and we are not able to apply the masking method reliably for these objects.

As the second method to estimate the total flux of an object, the MIRIAD program MBSPECT was used. The integrated H I spectrum of each detection was made, summing the flux in pixels contained in a box placed around the object and weighting the sum with the inverse value of the beam. The size of the box was estimated individually for each object based on the extent of the H I emission and was always slightly bigger than the object itself, both in the spatial and in the velocity domain. For the extended objects, which have IDs from 63 to 68, this was the only method used to estimate these two parameters. We mark the integrated fluxes obtained with MBSPECT $S_{\rm int,MBSPECT}$ and the corresponding peak values of the integrated profiles $S_{\rm peak,\,MBSPECT}$. In Fig. 5, the difference between integrated fluxes and peak fluxes measured using two different methods [(1) masking by defining pixels which belong to an object and (2) summing in a box using MBSPECT] is plotted. The difference is larger for the objects with lower values of integrated fluxes and integrated peak fluxes, where the influence of the noise in the flux values is relatively higher. Where possible, the average value from the two

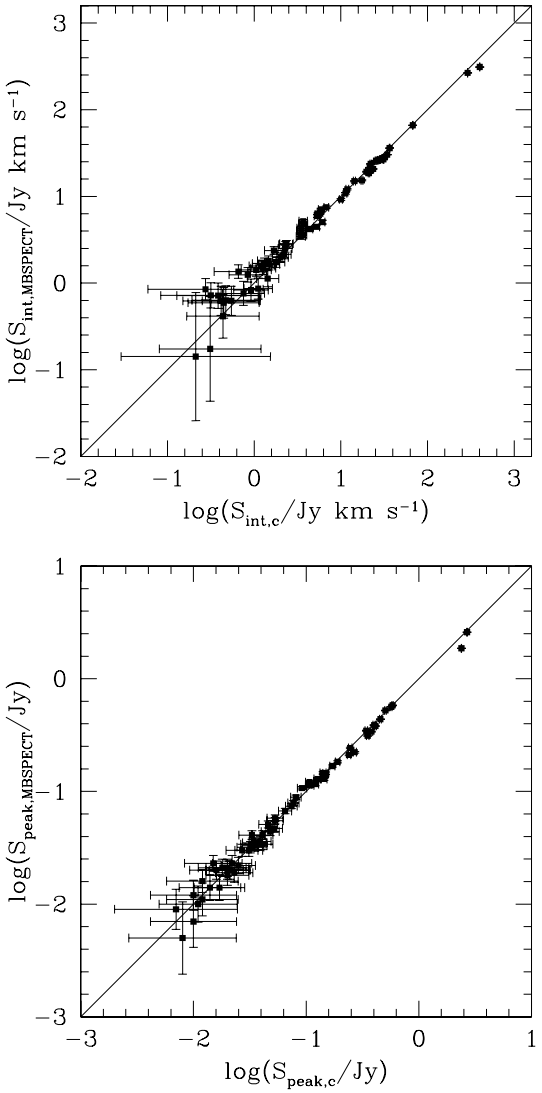

Figure 5. Comparison of the measured integrated flux (top) and integrated peak flux (bottom) values using two different methods for objects for which we have both measurements.The horizontal axis presents the measurements based on the flux values in the pixels defined to belong to an object (masking). The vertical axis presents the measurements using the MIRIAD task MBSPECT, defining the boxes around detections. The estimated errors for the presented parameters are described in Section 4.1.

methods used to estimate integrated flux ($S_{\rm int}$) and integrated peak flux ($S_{\rm peak}$) will be used as the final estimate of these two parameters for the detected H I objects.

The MIRIAD task MBSPECT was also used to parametrize the detections in velocity space. The widths of the profiles of the detections were measured at the 20 per cent ($W_{20}^{\rm obs}$) and 50 per cent ($W_{50}^{\rm obs}$) levels of the peak flux in the spectrum, using the methods of width maximization and minimization in MBSPECT. The maximization procedure measures the linewidths starting from the velocity limits given when specifying the box around a detection and moves inwards until the percentage of the peak flux is reached. The minimization procedure starts at velocity at which the profile has maximum and searches outwards. The velocities at the centres of the four measured profile widths were also estimated. The radial velocity of a detection was estimated as the average of those four measured velocities. The velocities in the datacubes and spectra were calculated from the observed frequencies ν using the radio convention $V_{\rm r} = c(1 - \frac{\nu}{\nu_0})$. The estimated systemic velocity was recalculated to the value in the optical convention $V_{\rm o} = c(\frac{\nu_0}{\nu} - 1)$. The velocities in the optical convention were recalculated from the geocentric to the barycentric frame. In addition, they have been corrected for the motion of the Sun around the Galactic Centre and the motion of the Galaxy in the LG using the expression (Yahil, Tammann & Sandage 1977)

$$V_{\rm LG} = V_{\rm o} + 296 \sin l \cos b - 79 \cos l \cos b - 36 \sin b, \quad (1)$$

which is similar to the IAU convention. In this formula $V_{\rm LG}$ is the LG velocity and l and b are the galactic coordinates of the detection.

The profile widths measured from the data have been corrected for instrumental resolution. We used method given by Verheijen & Sancisi (2001) to correct for broadening of the global H I profiles due to a finite instrumental velocity resolution. Assuming a Gaussian line shape for the edge of the profile, the slopes of which are determined by the turbulent motion of the gas with a velocity dispersion of 10 km s^{-1}, this correction can be written in the form

$$W_{20} = W_{20}^{\rm obs} - 35.8 \left[\sqrt{1 + \left(\frac{R}{23.5} \right)^2} - 1 \right] \quad (2)$$

$$W_{50} = W_{50}^{\rm obs} - 23.5 \left[\sqrt{1 + \left(\frac{R}{23.5} \right)^2} - 1 \right] \quad (3)$$

for the widths at 20 and 50 per cent of the peak flux, respectively. The observed widths $W_{20}^{\rm obs}$ and $W_{50}^{\rm obs}$ were calculated by averaging the 20 and 50 per cent level widths measured in the maximization and minimization procedure by MBSPECT. The instrumental velocity resolution R expressed in km s^{-1} was taken to be 33 km s^{-1}.

4 PARAMETER ACCURACY AND COMPLETENESS OF THE SURVEY

We use an empirical approach to assess the accuracy of the measured parameters of the detections and the completeness of the survey. Our method is based on inserting a large number of synthetic sources throughout the selected survey data. The major inputs to estimate the accuracy of the measured parameters are the recovered properties of the synthetic sources. The completeness of the survey is determined from the rate at which the synthetic sources could be recovered.

As a basis for the simulations, 10 line datacubes of full resolution were selected from the 1372 line datacubes produced in the whole survey. We refer to these datacubes as the basis datacubes. The datacubes selected were to our knowledge object free. Seven of the datacubes were selected from the central part of the area covered by the survey, while three of the datacubes were selected to be datacubes from the edges of the area covered by the survey; two of them are datacubes with one edge and one is a corner datacube with two edges.

The majority of the objects detected in the WSRT CVn survey are small H I objects, and the uncertainties and the completeness of these detections were the main focus for designing these simulations. The synthetic objects were created to resemble small H I objects, and therefore our simulations are not optimal for all possible types of H I objects. Five objects of different sizes in the spatial and velocity domains with different distributions of flux were created from the CLEAN components of H I objects detected in the survey. Created objects are two, three, four, five and six channels wide. The profiles of all the synthetic objects were also of triangular shape. In each of the basis datacubes, 10 objects were inserted and distributed quasi-randomly. Quasi-randomness in this context means that objects were inserted only in channels with positive velocities, as are all the real detections, and they were distributed in the datacube such as not to overlap with each other. It is possible that some overlapping sources could be partially accreted dark galaxies which show up only as asymmetries in single detections. Our small sources are too small with respect to the beam size to study their shapes in detail. For the large sources, this remains an unexplored possibility. The same synthetic objects were inserted at the same relative positions in all of the datacubes (same x, y and z of the three-dimensional datacube), in order to emphasize the influence of the underlying noise in the datacube on the measured properties of inserted objects. Obviously, the noise distribution differs from datacube to datacube. Before inserting the objects into the datacube, their flux was rescaled and they were convolved with the beam of the line datacube in which they were going to be inserted. Each of the synthetic objects was inserted in two positions in the datacube, with two different flux values. In total 10 runs were made, rescaling the maximum flux values two times for the five different model objects in each of the datacubes. In the first run of simulations, the maximum value of different model objects was fixed at 1.0 and 3.0 mJy, and in each of the following nine simulation runs the peak value was increased by 0.2 mJy. These flux values were chosen in such a way to ensure that there is a fraction of synthetic sources which will not be detected. In total 1000 different objects were inserted in 10 different datacubes.

The datacubes with inserted synthetic objects were then searched for these synthetic sources in a manner identical to the searching process used in the WSRT CVn survey, as described in Section 3.1. Detections which satisfied the criteria for real objects were parametrized the same way as the real detections, described in Section 3.2. The simulation described above was used to estimate the uncertainties of the measured H I parameters and the completeness of the WSRT CVn survey in the following two sections, respectively.

One of the shortcomings of our simulations is that all synthetic sources have profile widths of triangular shape. Zwaan et al. (2004) estimated parameter uncertainties and completeness of HIPASS (a single-dish survey) using synthetic sources of Gaussian (e.g. triangular), double-horned and flat-topped profile shapes. Within the errors, the completeness of the survey is the same for all types of profiles. Zwaan et al. (2004) did not discuss the uncertainties in the measured parameters on the profile shape.

4.1 Parameter uncertainties

The uncertainties of the H I parameters can be estimated from a comparison of the assigned and measured properties of the

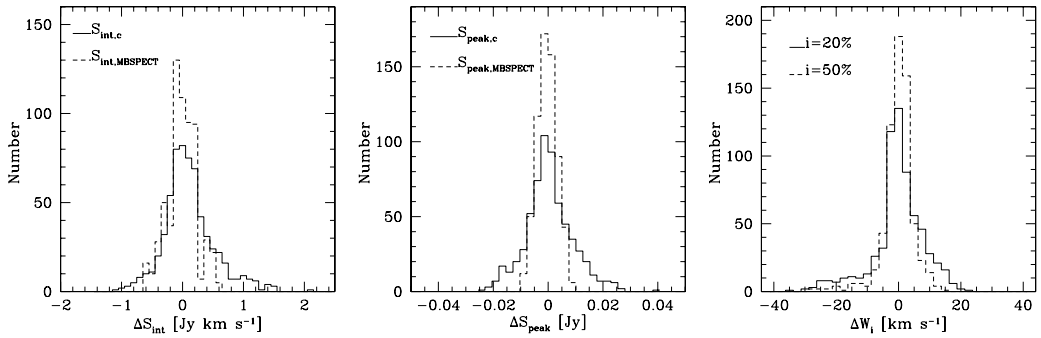

Figure 6. Comparison between inserted and measured parameters. The first two panels show the difference between the values of inserted parameters and parameters measured by forming a mask around a detection (full line histogram) and parameters measured with MBSPECT (dashed line histogram). The first panel shows the difference distribution for integrated flux values. The second panel shows the distribution of differences in integrated peak flux values. The third panel shows the difference between the inserted profile widths and recovered profile widths at 20 per cent of the maximum in a spectrum (full line histogram) and at 50 per cent of the maximum in a spectrum (dashed line histogram), measured with MBSPECT.

synthetic objects revealed in the simulated datacubes. In the simulations described above, 794 of the inserted 1000 synthetic sources were recovered using the searching criteria defined for the datacubes with the full resolution: at least 22 connected pixels with flux values larger than or equal to 4σ. Parametrization of the sources detected in the simulation was carried out and the distributions of differences between the real and the parametrized properties of the population of synthetic objects revealed in the simulation are presented in Fig. 6.

From the distributions of differences, the uncertainties of $S_{\rm int}$, $S_{\rm peak}$ and profile widths measured at 50 and 20 per cent of the line maximum were calculated as the standard deviation in the corresponding distributions. The uncertainties of the measured integrated fluxes in the WSRT CVn survey are $\sigma = 0.421\,{\rm Jy\,km\,s^{-1}}$ for the case of the flux summed inside the defined contour, $\sigma = 0.242\,{\rm Jy\,km\,s^{-1}}$ for the flux inside a box around a detection, while $\sigma = 0.240\,{\rm Jy\,km\,s^{-1}}$ for the flux of an object calculated as the average value measured from the two techniques used. For the integrated peak fluxes, uncertainties are $\sigma = 8.8, 3.7$ and 4.7 mJy for the three methods used, given in the same order as the $S_{\rm int}$ uncertainties above. Uncertainties for the profile widths (as observed) are $\sigma = 5.1\,{\rm km\,s^{-1}}$ and $\sigma = 8.4\,{\rm km\,s^{-1}}$ for the profile widths measured at 50 and 20 per cent, respectively.

The detectability of a 21-cm signal depends not only on the flux, but also on how this flux is distributed over the velocity width of the object of consideration. There is probably a more complicated dependence of the uncertainties of the estimated H I parameters on the intrinsic properties of an object. Given the relatively small number of detections in the WSRT CVn survey, we neglect such a dependence in our results. We only demonstrate the existence of the additional dependence of measured $S_{\rm int}$ values on the values of $S_{\rm int}$, $S_{\rm peak}$ and profile width. The results are presented in Fig. 7. Here, the difference $\Delta S_{\rm int}$ corresponds to the difference between the value of the integrated flux inserted and the integrated flux measured, calculated as the average value of the integrated flux obtained by using our program – defining a mask around a detection, and the integrated flux obtained by using the MIRIAD task MBSPECT – defining a box around a detection. The uncertainty of $S_{\rm int}$ is 0.130 Jy km s^{-1} in the range of true values $S_{\rm int} \leq 0.5\,{\rm Jy\,km\,s^{-1}}$ (continuous line in the left-hand panel in Fig. 7), $0.188\,{\rm Jy\,km\,s^{-1}}$ for $0.5 < S_{\rm int} \leq 1\,{\rm Jy\,km\,s^{-1}}$ (short dashed line), 0.280 Jy km s^{-1} for $1 < S_{\rm int} \leq 2\,{\rm Jy\,km\,s^{-1}}$ (dotted line) and 0.278 Jy km s^{-1} for $S_{\rm int} > 2\,{\rm Jy\,km\,s^{-1}}$ (long dashed line). To test the dependence of $\Delta S_{\rm int}$ on the $S_{\rm peak}$ value of the inserted detection, we split the $S_{\rm peak}$ values in the four arbitrary intervals: $S_{\rm peak} \leq 0.01$ Jy (continuous line), $0.01 < S_{\rm peak} \leq 0.02$ Jy (short dashed line), $0.02 < S_{\rm peak} \leq 0.04$ Jy (dotted

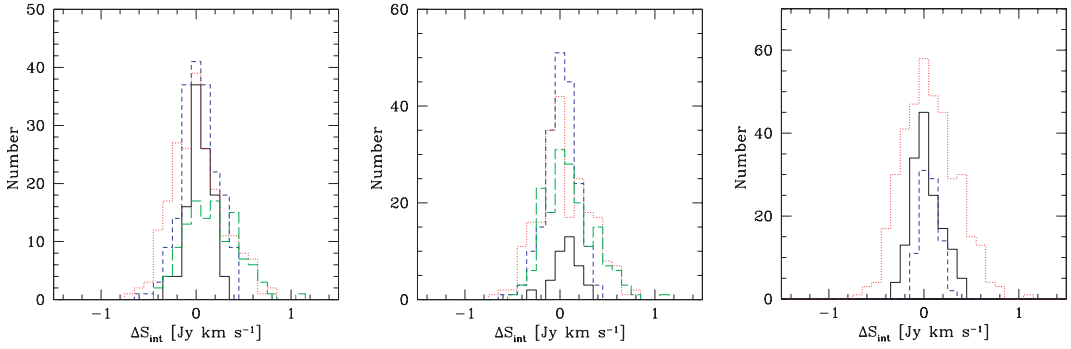

Figure 7. Distributions of $\Delta S_{\rm int}$, differences between the inserted integrated fluxes and detected integrated fluxes, as a function of inserted $S_{\rm int}$, $S_{\rm peak}$ and profile width. The detected $S_{\rm int}$ values are calculated as the average value of the integrated flux calculated by defining a mask around a detection and the integrated flux obtained by using the MIRIAD task MBSPECT, defining a box around a detection. In the left-hand panel, the continuous (black) line corresponds to the distribution of $\Delta S_{\rm int}$ for $S_{\rm int} \leq 0.5\,{\rm Jy\,km\,s^{-1}}$, the short dashed (blue) line is the same type of distribution for $0.5 < S_{\rm int} \leq 1\,{\rm Jy\,km\,s^{-1}}$, the dotted (red) line for $1 < S_{\rm int} \leq 2\,{\rm Jy\,km\,s^{-1}}$ and the long dashed (green) line for $S_{\rm int} > 2\,{\rm Jy\,km\,s^{-1}}$. The middle panel shows the distribution of $\Delta S_{\rm int}$ as a function of $S_{\rm peak}$. The continuous (black) line is for $S_{\rm peak} \leq 0.01$ Jy, the short dashed (blue) line for $0.01 < S_{\rm peak} \leq 0.02$ Jy, the dotted (red) line for $0.02 < S_{\rm peak} \leq 0.04$ Jy and the long dashed (green) line for $S_{\rm peak} > 0.04$ Jy. The right-hand panel shows the distribution of $\Delta S_{\rm int}$ as a function of W_{20} for the range of: $W_{20}^{\rm obs} \leq 45\,{\rm km\,s^{-1}}$ – continuous (black) line, $45 < W_{20}^{\rm obs} \leq 60\,{\rm km\,s^{-1}}$ – short dashed (blue) line and $W_{20}^{\rm obs} > 60\,{\rm km\,s^{-1}}$ – dotted (red) line.

line) and $S_{\rm peak} > 0.04$ Jy (long dashed line). The uncertainties are 0.134, 0.168, 0.278 and 0.265 Jy for the given intervals, respectively. Finally, we divided $\Delta S_{\rm int}$ values in the three intervals depending on the $W_{20}^{\rm obs}$ of the object. The uncertainty in $S_{\rm int}$ for the objects with: $W_{20}^{\rm obs} \leq 45\,{\rm km\,s^{-1}}$ (continuous line) is 0.156 Jy km s^{-1}, $45 < W_{20}^{\rm obs} \leq 60\,{\rm km\,s^{-1}}$ (short dashed line) is 0.091 Jy km s^{-1} and $W_{20}^{\rm obs} > 60\,{\rm km\,s^{-1}}$ (dotted line) is 0.285 Jy km s^{-1}.

4.2 Completeness

Completeness of the survey is the fraction of galaxies detected in a given volume down to the limiting sensitivity. The completeness of the blind WSRT CVn survey is addressed using the Monte Carlo simulations described. It is defined here as the ratio of the number of synthetic objects detected in the simulations and the number of synthetic objects inserted in the simulation.

The completeness of the survey is estimated as a function of $S_{\rm int}$ and $S_{\rm peak}$ values. To take into account all possible sources which would be detected in the real survey, datacubes with the inserted synthetic sources were smoothed in the spatial and velocity domain. The smoothing was identical to the smoothing of the real datacubes. The smoothed datacubes were searched in all resolutions applying the criteria as defined in Section 3.1. This resulted in the completeness corrections shown in Fig. 8 that were later applied in deriving the H I mass function.

The fraction of datacubes with one or two edges used in the simulations was much larger than the fraction of datacubes with edges in the real survey. To account for this, the completeness of the survey was estimated for each type of the datacube independently. The reason for including the datacubes with edges and testing them separately was that the noise distribution in the edge cubes is much more inhomogeneous. The completeness of the whole WSRT CVn survey was calculated weighting the number of detected objects with the relative abundance of the type of datacubes (in the survey) in which these objects were detected. The weighted completeness is considered to be the best estimate of the completeness of the whole survey. It is presented with the continuous line in Fig. 8. From the simulations carried out, it follows that the WSRT CVn survey is complete, at least in a statistical sense, for objects with approximately $S_{\rm int} > 0.9\,{\rm Jy\,km\,s^{-1}}$ and $S_{\rm peak} > 0.0175$ Jy. From 70 objects detected in the WSRT CVn survey, 12 of them have $S_{\rm int}$ values in the range for which the survey is incomplete. For only two detections the incompleteness is larger than 50 per cent. The minimum integrated flux of an object has to be 0.2 Jy km s^{-1} (centre of the first bin with a non-zero completeness) in order to be detected in the WSRT CVn survey.

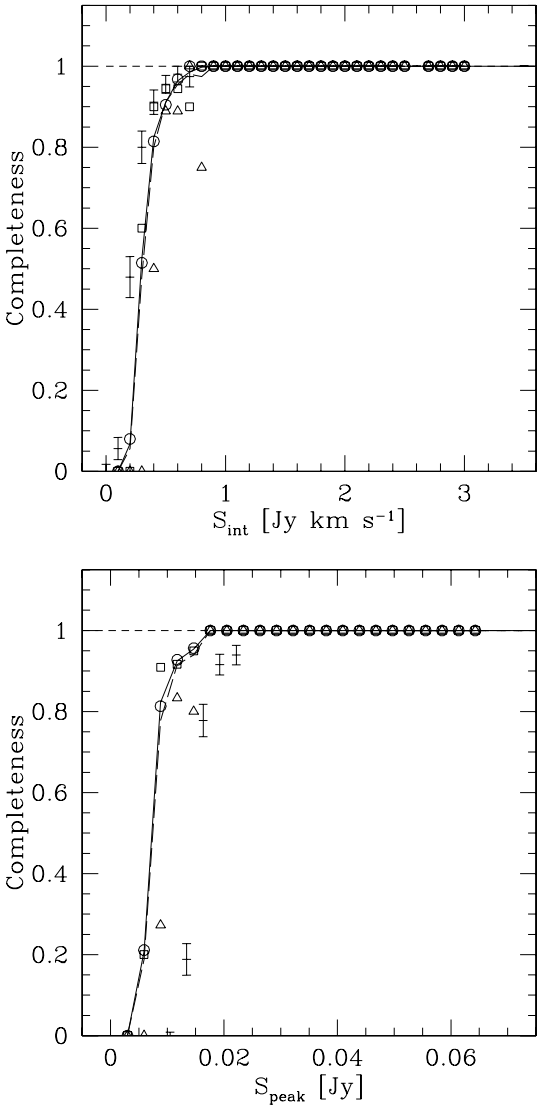

Figure 8. Completeness of the WSRT CVn survey. Circles represent the fraction of objects detected in the datacubes within the survey, without an edge. Squares correspond to the fraction of detected objects residing in the datacubes with one edge and triangles represent the fraction of objects detected in the datacubes with two edges. The continuous line connects the bins with a fraction of detected objects weighted with the relative abundance of a type of the datacube in which the detection resides. The long dashed line connects fractions of all objects detected in the simulation regardless of the type of the datacube in which the detection was inserted. The short dashed horizontal line represents the line for which the survey is complete. The errors are estimated from the binomial statistics. For clarity, the errors are presented only for the completeness based on all datacubes without weighting for the datacube type, and they are offset along the *x*-axis.

5 PROPERTIES OF THE H I DETECTIONS

5.1 Comparison of the detections with previous observations

The cross-correlation of the objects detected in the WSRT CVn blind survey with known objects was conducted using the NASA/IPAC Extragalactic Data base (NED). Both positional and velocity information, if available, were used to identify a counterpart of each of the detected H I sources. In addition, the Lyon/Meudon Extragalactic Data base (HYPERLEDA) was used and the second-generation Digital Sky Survey (DSS) images, centred on the position of the WSRT CVn detections, were visually inspected. We also inspected the SDSS images. We used the SDSS object identification and their redshift, if obtained, only in combination with the visual inspections of the images of cross-correlated galaxies, or parts of them, because of the not yet fully resolved problem with deblending of the extended sources (e.g. West 2005; http://www.sdss.org/dr7/products/catalogs/index.html#cav_lowlat).

In total, 67 objects detected in the WSRT CVn survey were identified as galaxies previously detected in one of the optical wavebands. The cross-correlation is based on both the positional and velocity information for 58 objects. Objects WSRT-CVn 67A and WSRT-CVn 67B were cross-identified with two galaxies based on position and redshift information in the literature: NGC 4490 and NGC 4485, respectively. Using our data, we were not able to separate the 21-cm

emission detected around WSRT-CVn 67A and WSRT-CVn 67B into two individual detections. Object WSRT-CVn 34 (UGCA290) looks like an interacting binary system, addressed as such in some references. We consider it as one object, a patchy dwarf galaxy, based on the resolved stellar photometry carried out by Makarova et al. (1998).

For the remaining nine H I detections (WSRT-CVn 8, 13, 17, 19, 25, 30, 31, 47 and 55), the cross-correlation with the previous detections is based solely on the positional information of the assigned optical counterparts. Given that these galaxies are best visible in blue light and ∼10–20 arcsec in size, it is most probable, even without knowing their redshifts, that they are the optical counterparts of the H I detections. Close to the position of two additional H I detections, galaxies are visible in both DSS and SDSS images. One of these galaxies (which overlaps WSRT-CVn 42) is detected in the SDSS splitted into multiple detections (in the currently last available SDSS data release 7), therefore there does not exist a uniquely previously identified galaxy for this H I object. Two blue galaxies are detected in the area of the projected H I of WSRT-CVn 40 (see Appendix A). One of these galaxies has the SDSS measured redshift $z = 0.029$, which completely disqualifies it as a possible contributor to the detected H I. We cross-correlate therefore WSRT-CVn 40 with the other galaxy. This galaxy is not detected by the SDSS pipeline, probably due to its proximity to a star.

An important question related to the cross-correlation of objects when using only positions and some properties of galaxies is what is the probability that this H I–optical pair is only a chance projection. The geometric probability P that a galaxy of magnitude m and at angular distance θ from the studied galaxies is only a chance projection (neglecting the correlation properties of galaxies) is given by (e.g. Wu & Keel 1998)

$$P(\theta, m) = 1 - \exp(-\pi\rho(m)\theta^2), \quad (4)$$

where $\rho(m)$ is the surface number density of galaxies brighter than m. We obtained the surface number density of galaxies from the SDSS data base by counting the number of galaxies within 11 randomly placed pointings of a radius of 30 arcmin in the WSRT CVn survey region. Properties of galaxies were selected to resemble the properties of the secure host galaxies of the faint H I detections. Roughly, we have taken $16 < r < 20$ mag and $0.2 < g - r < 0.6$ (see chapter 5 in Kovač 2007). We measured the density of galaxies with these properties to be about 52 per pointing, leading to a probability that the cross-correlated optically identified galaxy is only a chance projection of 0.056 or 0.00014, if the optical detection is at a distance of 1 or 0.5 arcmin, respectively, from the H I detection. From the inspection of the images of the H I overlaid on the top of the optical counterpart, it is clear that the projected distances between the optical detection and the maximum in the H I surface density are less than 1 arcmin. We conclude that our cross-correlations without the known distances of the optically detected galaxies are also pretty secure. Moreover, our measurements provide first measurements of distances to these galaxies.

Finally, based on the inspection of the DSS and SDSS images, there was one object detected in H I without an optical counterpart (WSRT-CVn 61). This object is found a few arcmin away and within ∼110 km s^{-1} from NGC 4288 (WSRT-CVn 62). This object has already been detected in H I by Wilcots, Lehman & Miller (1996) in H I observations of a sample of five barred Magellanic spiral-type galaxies. Interestingly, Wilcots et al. (1996) detected similar H I clouds, without an obvious optical counterpart on the DSS images, and with the H I mass $\sim 10^7$ M$_\odot$ in four out of five galaxies in their sample. In our data, WSRT-CVn 61 is barely resolved (see Appendix A), but clearly distinguished from NGC 4288 in the velocity. It has a single-peaked global H I profile, consistent with a very weak rotation ($W_{50} \sim 20$ km s^{-1}).

Potentially, detecting a dark object is very interesting in the context of this paper. We have carried out a follow-up optical observation in the field of NGC 4288, using the Wide Field Camera on the Isaac Newton 2.5-m telescope, La Palma, Canary Islands. The observations did not reveal any sign of the stellar light nearby the position of WSRT-CVn 61 down to the surface brightness limit of 26.3 mag arcsec^{-2} in R and 27.4 mag arcsec^{-2} in B (Kovač 2007, chapter 5). The observations will be presented in more details in a future paper. To conclude, the nature of WSRT-CVn 61 is not entirely clear, but given its proximity to NGC 4288, it is likely to be a very LSB companion to this galaxy. We treat it as a separate object.

The homogenized H I data (HOMHI) catalogue (Paturel et al. 2003) represents a compilation of H I detections from 611 papers. This catalogue was used to inspect the whole volume covered by this survey for previous H I detections. According to the HOMHI catalogue, there are 47 objects which have been observed in the 21-cm line inside the volume of the WSRT CVn survey, and four objects are at the edges of the observed region (objects with WSRT-CVn indexes 1, 2, 60 and 62). Of the 47 HOMHI detections inside the survey volume, 44 can be cross-correlated uniquely with the WSRT CVn detections using their position on the sky and their heliocentric velocities. One of the detections of the WSRT CVn survey (WSRT-CVn 23) is cross-correlated with two objects in the HOMHI catalogue. These two HOMHI detections have the same heliocentric velocity, and their positions differ by 0.°015 and 0.°14 in right ascension and declination, respectively. Their profile widths are identical and their $S_{\rm int}$ values are almost the same. From tracing these detections back in the literature, it follows that their names have been confused; there is only one object detected with the given H I properties and velocity.

One of the HOMHI detections does not have a counterpart in the WSRT CVn survey. That is MAPS-NGP O_218_0783987, with heliocentric velocity 636 km s^{-1}. Huchtmeier et al. (2000) measured $S_{\rm int} = 0.66$ Jy km s^{-1}, $S_{\rm peak} = 0.026 \pm 0.0046$ Jy, $W_{50} = 27$ km s^{-1} and $W_{20} = 34$ km s^{-1} for this object, using the single-dish 100-m radio telescope at Effelsberg. The WSRT CVn survey is slightly incomplete ($C > 90$ per cent) for the $S_{\rm int}$ value and complete for the $S_{\rm peak}$ value of this object. We carefully examined the datacube from the WSRT CVn survey produced at the position of MAPS-NGP O_218_0783987. There is no sign of the 21-cm emission at that position in our data. Based on the cross-correlation with the previous observations, all detections from the WSRT CVn survey are real. We are inclined to believe that the detection in the Huchtmeier et al. (2000) sample is not real, but is, perhaps, interference.

There is no entry in the HOMHI catalogue for objects WSRT-CVn 9 and WSRT-CVn 61. HYPERLEDA, however, provides H I data for WSRT-CVn 9. For a comparison with the literature, we used the measurement from Wilcots et al. (1996) for object WSRT-CVn 61. Object WSRT-CVn 7 has been listed in the HOMHI catalogue, but without a measurement of integrated flux. We obtained the $S_{\rm int}$ value for WSRT-CVn 7 from Matthews & van Driel (2000). This $S_{\rm int}$ value has been corrected for the finite size of the Nançay telescope beam. In total, from 70 detected H I sources in the WSRT CVn survey, 19 have been detected for the first time in the 21-cm emission line in this survey.

In Fig. 9, the comparison of $S_{\rm int}$ values measured in the WSRT CVn survey and $S_{\rm int}$ values available from the literature is presented. For objects with the WSRT-CVn indexes 7 and 61, we use

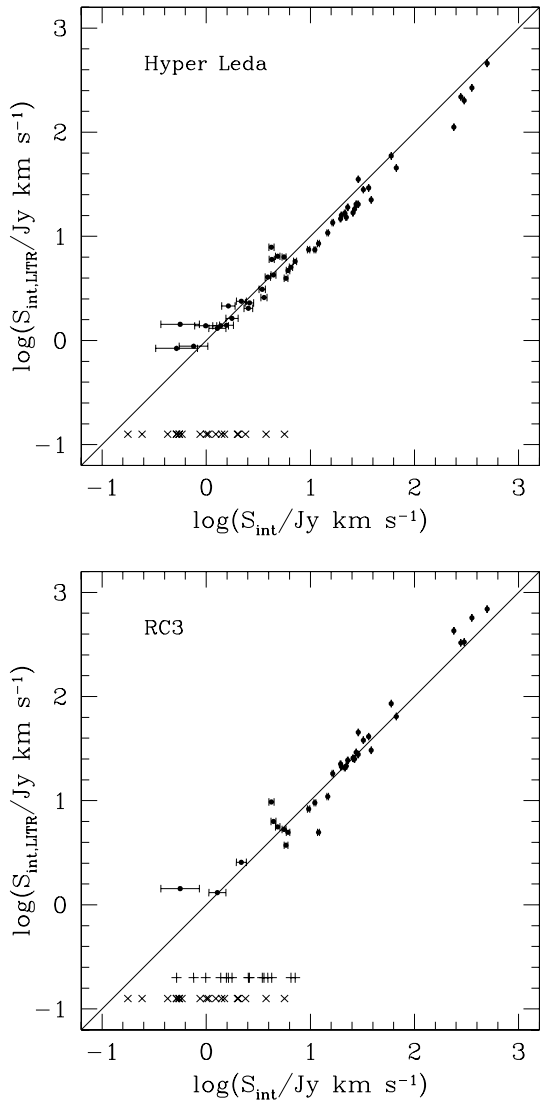

Figure 9. Comparison of the WSRT CVn $S_{\rm int}$ values with literature measurements. For WSRT-CVn 7 and WSRT-CVn 61 $S_{\rm int}$, literature measurements come from Matthews & van Driel (2000) and Wilcots et al. (1996), respectively. In the top panel, literature values of integrated fluxes obtained from HYPERLEDA have been used. In the bottom panel, integrated fluxes published in RC3 have been used. The integrated flux values of objects for which there is no previous H I measurement in the literature have been indicated with an 'x' symbol. $S_{\rm int}$ values of detections without RC3 measurements, but for which the $S_{\rm int}$ value in the HOMHI catalogue is available, have been indicated in the bottom panel with a '+' symbol. We plot the errors only for our measurements.

the values from the references given above. For the comparison presented in the top panel in Fig. 9, we used the $S_{\rm int}$ values retrieved from HYPERLEDA for the rest of the objects. It is obvious that the HYPERLEDA integrated fluxes are systematically smaller than the WSRT CVn integrated fluxes for approximately $S_{\rm int} > 10\,{\rm Jy\,km\,s^{-1}}$. The $S_{\rm int}$ values in HYPERLEDA come from the HOMHI catalogue (with the exception of object WSRT-CVn 9) and the majority of them have been measured with a single-dish telescope. We have not traced back in the literature the references for the individual detections from the HOMHI catalogue. Instead, we collected $S_{\rm int}$ values for the WSRT CVn detections from the earlier RC3 catalogue (de Vaucouleurs et al. 1991). These two catalogues (HOMHI and RC3) are not independent. The comparison between the integrated flux values measured in the WSRT CVn survey and the literature $S_{\rm int}$ values collected from the RC3 catalogue, and for the objects with the IDs 7 and 61 from the individual papers, is presented in the bottom panel in Fig. 9. The RC3 catalogue contains $S_{\rm int}$ values for fewer objects detected in the WSRT CVn survey than the HOMHI catalogue. Still, most of the objects with $S_{\rm int}$ values above 10 Jy km s^{-1} are present in both catalogues considered. There is no systematic difference between the WSRT CVn integrated fluxes and the RC3 integrated fluxes. It is possible that the systematic offset seen between our values of the integrated fluxes and those in the HOMHI catalogue is due to the corrections applied in the homogenization process of the H I data used to create the H I parameters provided in the HOMHI catalogue. This difference can arise also from the distribution of H I in a galaxy. We use the interferometric data, and we are restricted to the flux measurements in the galaxies. If a galaxy has a lot of outlying H I, we are not sensitive to include it, while the single-dish observation picks it up. Given that our measurements agree with the RC3, we use the RC3 measurements of $S_{\rm int}$, heliocentric velocity, W_{50} and W_{20} for objects WSRT-CVn 67A and WSRT-CVn 67B, for which we cannot properly measure the H I properties from the WSRT CVn survey data.

5.2 Distributions of H I properties of the detections

The various distributions of the measured parameters of objects detected in H I in this survey can be used to examine the basic properties of the detected sample. Histograms of the distributions with radial velocity, integrated flux, peak flux and profile width at the 50 per cent level of the maximum flux in the spectra are shown in Fig. 10.

The redshift distribution of the detected objects is presented in the top-left histogram. A fraction of 29 per cent of all detections fall in a 100 km s^{-1} wide interval with velocities $525 \leq cz \leq 625\,{\rm km\,s^{-1}}$. This peak coincides with the peak of the CVnII cloud (Tully &

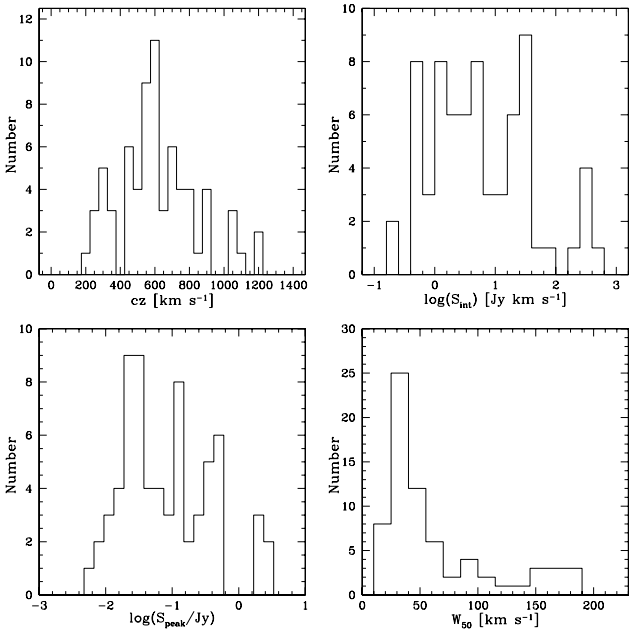

Figure 10. Distributions of estimated H I parameters. Histograms show the number distribution of the WSRT CVn detections in bins of cz (top left), $S_{\rm int}$ (top right), $S_{\rm peak}$ (bottom left) and W_{50} (bottom right).

Fisher 1987). The peak of the CVnI cloud is at $\sim$300 km s^{-1} (Tully & Fisher 1987), clearly identifiable in the histogram of observed redshifts.

The distribution of measured $S_{\rm int}$ values is shown in the top-right panel of Fig. 10. The detections with values $S_{\rm int} \geq 80$ Jy km s^{-1}, six in total, are excluded from the plot. The distribution of $S_{\rm peak}$ values is presented in the bottom-left panel of Fig. 10. Most of the objects detected in the WSRT CVn survey have the small $S_{\rm int}$ and $S_{\rm peak}$ values measured. For example, a fraction of 63 per cent of the detected objects have $S_{\rm int} \leq 10$ Jy km s^{-1}, while 72 per cent of the detections with available $S_{\rm peak}$ measurements have $S_{\rm peak} \leq 0.2$ Jy.

The last panel, bottom right in Fig. 10, corresponds to the distribution of the profile widths at the 50 per cent level of the maximum flux in the spectra of the detected objects, W_{50} (corrected for the instrumental effects). This distribution has a prominent peak around $W_{50} \sim 35$ km s^{-1}. 86 per cent of the detected H I objects have $W_{50} \leq 130$ km s^{-1} and can be considered as a candidate population of dwarf galaxies [Duc et al. (1999) found that 75 per cent of galaxies selected by the same profile width criteria are genuine dwarf galaxies]. However, the observed profile widths are affected by the inclination of a galaxy, and we discuss this issue in more detail in Section 5.3.

The bivariate distributions of velocity, profile width, peak flux, integrated flux and size are shown in Fig. 11. Objects detected for the first time in H I in this survey are marked with open symbols. It is clearly visible that the newly detected H I objects have small integrated fluxes and integrated peak fluxes, small profile widths and small physical sizes.

The log–log plot of $S_{\rm peak}$ versus $S_{\rm int}$ demonstrates the simple property that H I detections with larger integrated fluxes have higher

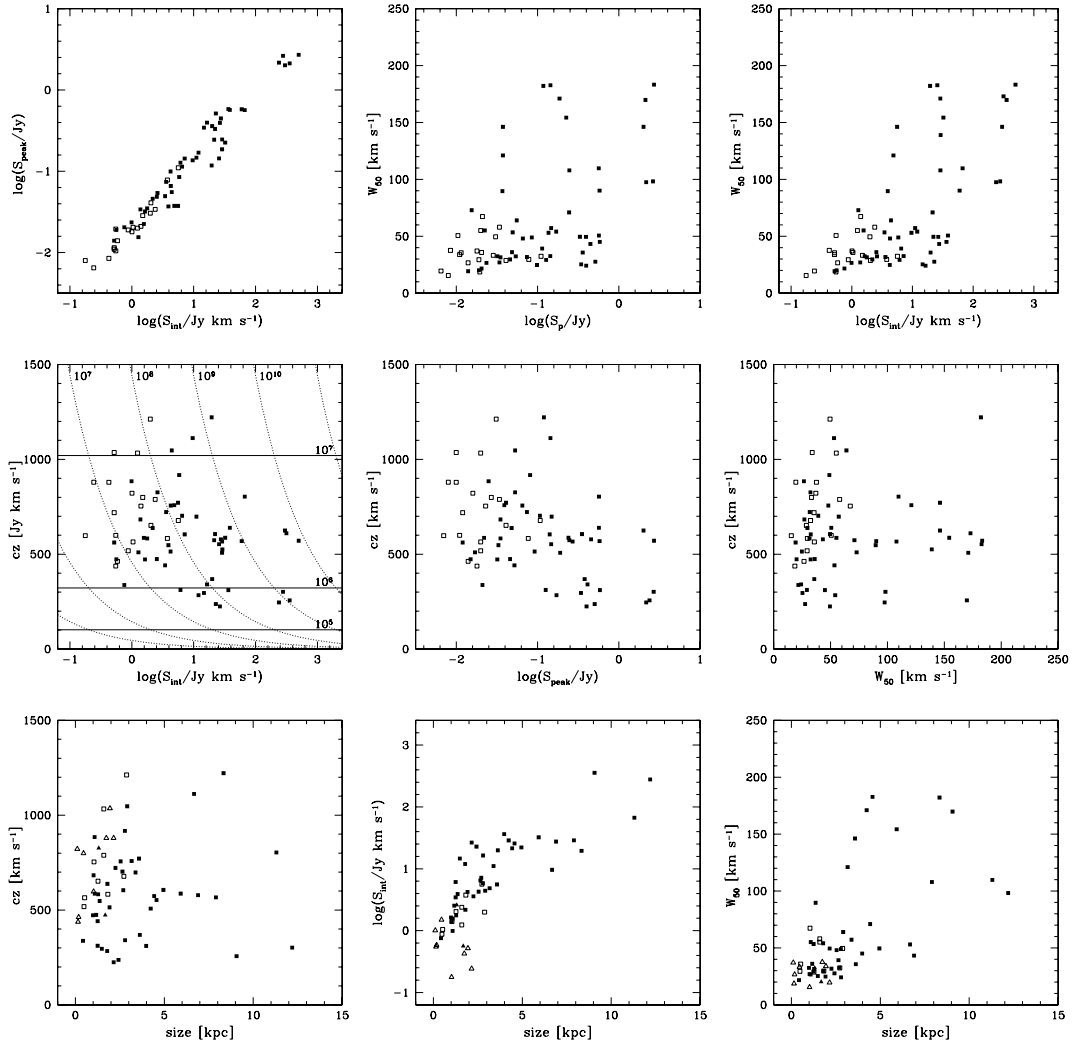

Figure 11. Bivariate distributions of observed parameters: $S_{\rm int}$, $S_{\rm peak}$, W_{50}, cz and H I size. The objects detected for the first time in the 21-cm emission line in the WSRT CVn survey have been presented with open symbols; the remaining objects are marked with filled symbols. In the plots in the bottom row, objects for which size is estimated from the isophote at a column density level of 1.25×10^{20} atoms cm^{-2} are marked with squares; if their size is estimated from a Gaussian fitted to the H I distribution they are marked with triangles. In the plot in the middle-left panel, lines of a constant H I mass are shown (dotted lines). The H I mass of a detection (in $M_\odot$) has been calculated assuming an optically thin approximation, $M_{\rm HI} = 2.356 \times 10^5 d^2 S_{\rm int}$, for $S_{\rm int}$ expressed in Jy km s^{-1} and d being the distance to an object in Mpc. We assumed $d = cz/H_0$, and used $H_0 = 70$ km s^{-1} Mpc^{-1}. The lines of constant H I mass in $M_\odot$ are presented with a logarithmic step of 1. The horizontal continuous lines represent the maximum recession velocity up to which an object of a certain H I mass can be detected in the WSRT CVn survey. We used the same assumption about the distance to an object as described above. The minimum detectable integrated flux in the WSRT CVn survey is 0.2 Jy km s^{-1}, obtained from the calculations of the completeness of the survey. However, we are complete only for $S_{\rm int}$ measurements above 0.9 Jy km s^{-1}.

integrated peak fluxes and vice versa. It is interesting that this relation holds for the detections over the whole range of observed integrated fluxes and integrated peak fluxes. The bivariate distributions of W_{50} versus $S_{\rm int}$ or $S_{\rm peak}$ show that there are no galaxies with large W_{50} with small integrated fluxes and low integrated peak fluxes in the volume probed. Objects with small integrated fluxes spread over large profile widths (if they exist) would be very difficult to detect. Similarly, low $S_{\rm peak}$ galaxies with large profile widths cannot be detected because the flux is in the noise. Smoothing in the velocity domain increases the sensitivity to this type of objects. However, smoothing the datacubes in the WSRT CVn survey in the velocity domain did not reveal any new detections.

The distributions of measured H I parameters with redshift (cz) show a segregation of detections in two groups, reflecting the positions of the CVnI and CVnII clouds in redshift space. In the redshift distributions of $S_{\rm int}$ and $S_{\rm peak}$, there appears to be an absence of detections with small $S_{\rm int}$ (and small $S_{\rm peak}$) at low cz, also in that part of parameter space for which the survey is complete. The survey by itself does not have any selection effects which would bias it against the detection of objects in the nearby Universe with small integrated fluxes. As already discussed in Section 5.1, comparing our detections with previous H I observations reveals that there are no H I objects with $cz \leq 400\,{\rm km\,s^{-1}}$ which have been missed in the WSRT CVn survey. Therefore, the absence of an H I population with $S_{\rm int} \leq 6\,{\rm Jy\,km\,s^{-1}}$ (or $S_{\rm peak} \leq 0.1$ Jy) is real. However, taking a flat H I mass function and the number of detected objects in the higher mass bin 10^7–$10^8\,{\rm M}_\odot$ (5), one would expect $5 \pm \sqrt{5}$ objects in the 10^6–$10^7\,{\rm M}_\odot$ bin, which is not too inconsistent. Moreover, the volume of the survey region limited with $85 < cz < 322.5\,{\rm km\,s^{-1}}$ is less than $1\,{\rm h_{70}^{-3}\,Mpc^3}$. The observed redshift distributions of $S_{\rm int}$ and $S_{\rm peak}$ probably reflect just a peculiarity of the CVnI group.

In addition, we present the bivariate distributions of cz, $S_{\rm int}$ and W_{50} as a function of size of those objects for which the size was estimated. We used the average value of the major and minor axes estimated at a column density level of 1.25×10^{20} atoms cm^{-2}, or only the FWHMs along the major and minor axes of a Gaussian fitted to the small detections. To express the size in kpc instead of arcsec, we have adopted distances d to the objects calculated from $d = cz/H_0$ using $H_0 = 70\,{\rm km\,s^{-1}\,Mpc^{-1}}$.

To get an idea which part of the space of H I parameters is explored in the WSRT CVn survey, the measured properties of objects detected in this survey are compared to the properties of objects detected in the southern $\delta < 2^\circ$ part of the H I Parkes All Sky Survey (HIPASS; Barnes et al. 2001; Meyer et al. 2004). Bivariate distributions of $S_{\rm int}$, $S_{\rm peak}$ and $W_{50}^{\rm obs}$ are plotted in Fig. 12. Values of $W_{50}^{\rm obs}$ used in the comparison have not been corrected for instrumental resolution, with the exception of the objects with WSRT-CVn IDs 67A and 67B, for which the $W_{50}^{\rm res}$ values obtained from the literature have been already corrected for the finite spatial resolution of the H I observations. The beam size of the HIPASS survey is 15.5 arcmin. It can be expected that due to the large size of the beam some of the HIPASS detections correspond to multiple objects. From the comparison of integrated fluxes and integrated peak fluxes of the detections from the two blind H I surveys, it follows that the WSRT CVn survey reveals H I objects with $S_{\rm int}$ and $S_{\rm peak}$ about 10 times smaller than the smallest HIPASS detections. This confirms our ability to detect objects which are faint in H I. The relative number of small mass objects (objects with small velocity widths; see in

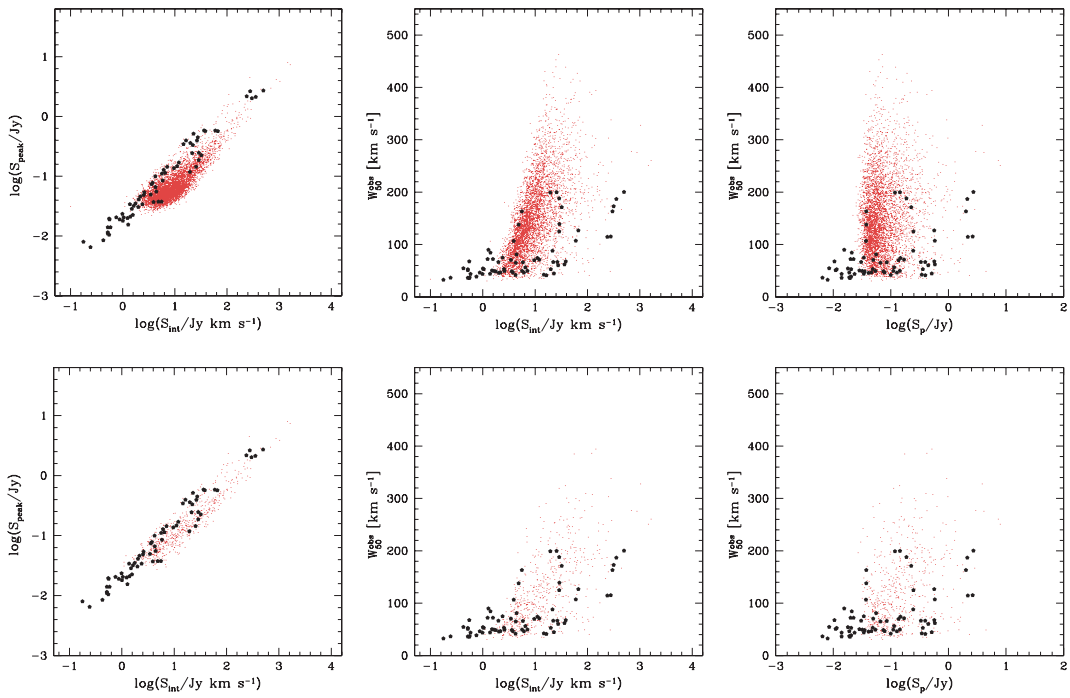

Figure 12. Comparison with the HIPASS detections. Small dots represent the HIPASS measurements. Big filled pentagons correspond to the WSRT CVn measurements. Profile widths have not been corrected for instrumental resolution, except for the objects WSRT-CVn 67A and WSRT-CVn 67B for which the literature values of profile widths, already corrected for instrumental broadening, have been used in the middle panels. The properties of the WSRT CVn detections are compared with the properties of the all HIPASS detections in three upper panels and with the properties of a subset of the HIPASS detections limited with $V_{\rm LG} \leq 1400\,{\rm km\,s^{-1}}$ in three lower panels, respectively. We detect very few big objects, i.e. galaxies with broad profiles and low $S_{\rm peak}$ but large $S_{\rm int}$ (when integrated over velocity). At larger distances, these start to dominate the sample. The comparison with the near galaxies in HIPASS in the bottom-left panel clearly underlines this.

Section 5.3 discussion on the effect of the inclination) in the WSRT CVn survey is much larger when compared to the relative amount of low-mass systems detected in HIPASS. On the other hand, large (massive) galaxies have not been detected in the volume covered by the WSRT CVn survey. All detections in the WSRT CVn survey have $W_{50}^{\rm obs} \leq 200\,{\rm km\,s^{-1}}$, while the detection with the broadest profile in the HIPASS has $W_{50}^{\rm obs} \sim 460\,{\rm km\,s^{-1}}$. This is expected for the volume covered by the WSRT CVn survey because the H I MF is a Schechter function with a flat faint-end slope. The WSRT CVn survey samples with high sensitivity a specific region of the sky up to a distance corresponding to $cz \sim 1330\,{\rm km\,s^{-1}}$, known to be populated by small, gas-rich galaxies at small distances. The HIPASS survey goes much deeper, up to $cz \sim 13\,000\,{\rm km\,s^{-1}}$, and covers a variety of environments. Therefore, for an easier comparison, we include the same type of plots for the subset of HIPASS detections limited with $V_{\rm LG} \leq 1400\,{\rm km\,s^{-1}}$. Here, we mainly want to point out that the WSRT CVn survey has a much lower flux limit $S_{\rm int}$ than HIPASS.

5.3 Effects of the inclination

In this section, we discuss the importance of the inclination of the objects on the results presented. We use the sizes of the objects measured from the H I images, assuming intrinsically circular symmetry, to obtain the inclination i of an object according to $\cos i = (b/a)$. Because some objects are very small or have patchy H I distributions, the derived inclinations are only indicative (i.e. they are very uncertain). However, our main goal here is to discuss the influence of the inclination of galaxies to the results presented so far: to the measured velocity widths and to understand if we have missed some H I objects because of inclination effects. From the *b*/*a* distribution (see discussion below), it appears that the errors in the measured inclinations are random (due to the noise in the data) and not systematic. We believe that for our purpose the inclinations measured from the H I data should be sufficient.[1]

As described in Section 3.2, we estimated the H I sizes for 61 objects detected in the survey. For two additional objects, we used the FWHM of a fitted Gaussian, not deconvolved for the synthesized beam as these objects were too small. The histogram of the H I axis ratios *b*/*a* of the detections is presented in Fig. 13. The distribution of *b*/*a* ratios of a sample of infinitely thin and round discs projected randomly on the sky will be flat (Hubble 1926). It is clear that the distribution of *b*/*a* values for the galaxies in this survey is not flat, also when considering Poisson errors in the *b*/*a* bins, and we need to understand why this is the case.

An important question is if there is a population of H I galaxies which has been missed in the survey due to their specific inclination. Could the WSRT CVn survey miss galaxies with both small and large *b*/*a* ratios? Apart from the errors in estimating the H I diameters of the detected objects, there are two additional effects which can cause the observed *b*/*a* distribution. First, *b*/*a* cannot equal 1 if discs are not circular. For example, the average face-on system in the complete sample of Sb–Sc galaxies selected from European Southern Observatory (ESO)-LV survey has $b/a \sim 0.7$ (Valentijn 1994). Secondly, if a galaxy has a finite thickness z, it means that there is a minimum *b*/*a* value, and one should see an excess of galaxies at that value (equal to z/a) and a deficit below that value. The H I discs are of finite thickness and the lack of detections with low *b*/*a* ratios probably reflects this effect. So, qualitatively, we can explain both deficits in the histogram of *b*/*a* ratios of the H I distributions. The conclusion then is that there is no population of H I objects with large and small *b*/*a* ratios which has been systematically missed in the survey.

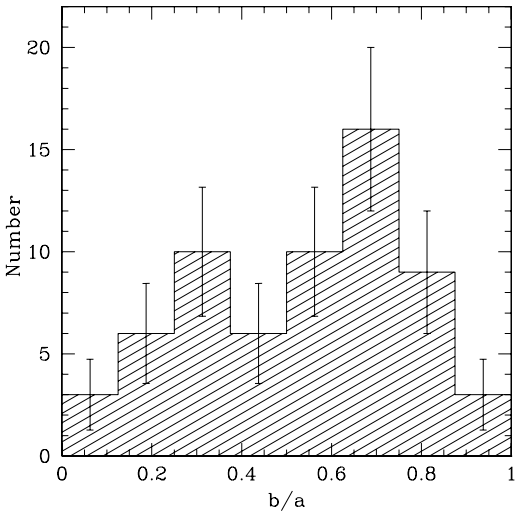

Figure 13. Histogram of *b*/*a* ratios for 63 objects detected in the WSRT CVn survey. *a* and *b* values are obtained from the H I data.

Quantitatively, this conclusion (no systematically missed detections) is confirmed by the previous H I observations carried out in the volume probed by the WSRT CVn survey. The CVnI cloud is nearby and a large number of observations have been carried out in this region, sometimes with much longer integration times. However, every single H I object detected previously in the nearby Universe ($cz < 600\,{\rm km\,s^{-1}}$) has been detected in the WSRT CVn survey. According to the existing data bases, only one of the known H I sources has been (maybe) missed in the total volume of the survey.

From the H I parameters measured for the detections from the WSRT CVn survey, the profile width is the only quantity which depends on the inclination. The profile widths presented in the previous sections are not corrected for the inclination – in reality, the profile widths should be corrected with a factor of $(\sin i)^{-1}$. Fig. 14 shows the distribution of profile widths measured at 50 per cent of maximum in the spectra and corrected for the inclination derived from the H I maps, $W_{50,i}$. In total, there are 63 detections with measurable inclination from the H I axis. Due to the small inclination, detection WSRT-CVn 35 is omitted from the plot. Generally, detections spread more along the profile width axis when compared to the corresponding distribution of profile widths not corrected for inclination (right-hand panel in the middle row in Fig. 11). However, still 78 per cent of all galaxies with measured *b*/*a* ratios have $W_{50,i} \leq 130\,{\rm km\,s^{-1}}$. There is no drastic change in the overall results obtained by correcting the profile widths for the inclination.

6 SUMMARY

We have carried out a blind H I survey with the WSRT in the volume of the nearby CVn groups of galaxies. The survey covers an area on the sky of ∼86 deg^2 and a velocity range of approximately $-450 \leq cz \leq 1330\,{\rm km\,s^{-1}}$ wide. In the volume probed by the survey,

[1] We have also measured inclinations from the optical data. For example, the Spearman correlation coefficient between the inclinations measured from the WSRT CVn H I data and the SDSS data is 0.41. We used a finite disc thickness of 0.2.

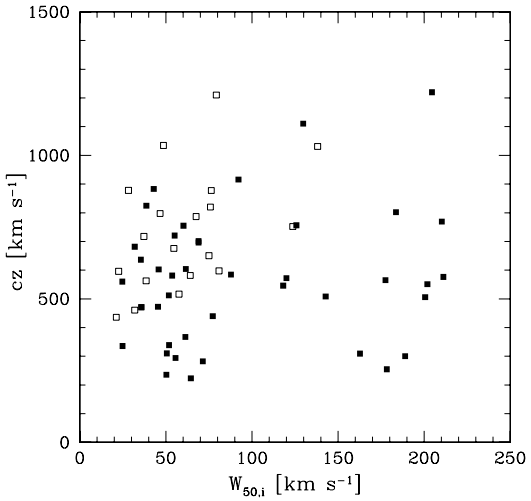

Figure 14. Bi-variate distribution of the inclination-corrected $W_{50,i}$ values and recession velocity. The open symbols are detections with H I measurements obtained for the first time in this survey. The filled symbols correspond to the detections with existing H I data in the literature.

we detect 70 H I objects. Using available data bases, 69 of the detections can be cross-correlated with a galaxy detected in the optical wavelength. Two galaxies cannot be resolved (WSRT-CVn 67A and WSRT-CVn 67B). One of the detections (WSRT-CVn 61) does not have an optical counterpart. This H I cloud resides in the proximity of NGC 4288 (WSRT-CVn 62).

We did not detect any isolated H I object without optical counterpart above the detection limit of the survey (see column 6 in Table 2). This result is in agreement with previous H I observations, each of them limited by their own detection limit (see Table 1) and with the recent theoretical work of Taylor & Webster (2005). According to their finding, all galaxies, whether dark or dim, would be detectable in H I. In all but one model studied, dark galaxies would undergo some star formation and therefore they would be detectable at optical wavelengths.

We estimated the various H I parameters of the detected objects. The uncertainties in the parameters are discussed in Section 4.1. The parameters measured are presented in Tables 3 and 4. The columns in Table 3 are defined as follows.

Column (1) – object's ID in the WSRT CVn survey.

Column (2) – name of the galaxy associated with the H I detection, taken from NED.

Column (3) – morphology of the galaxy, taken from HYPERLEDA. There is no morphological classification for objects with WSRT-CVn IDs 29, 30 and 34 in HYPERLEDA. For these three objects we provide the morphology from NED. Object WSRT-CVn 31 has been classified in NED as a galaxy of type dE4, which is obviously wrong, and we omit this result. Objects without a morphological classification either in HYPERLEDA or in NED have been marked with '−'.

Columns (4) & (5) – right ascension and declination, respectively, of the galaxy taken from NED. For objects without an associated object in the NED data base (objects with WSRT-CVn IDs 25, 40, 42, 55 and 61), the position of the centre of an ellipse, fitted to the H I map of the object, has been given.

Columns (6) & (7) – FWHM of a two-dimensional Gaussian fitted to the dirty beam of a datacube which contained the detection, expressed in arcsec.

Column (8) – position angle, in degrees, of a two-dimensional Gaussian fitted to the dirty beam of a cube which contained detection.

Column (9) – indicator of previous H I observations: 1 stands for previous H I observations available in the literature and 0 if otherwise.

A column description of the H I properties listed in Table 4 is given below.

Column (1) – WSRT-CVn ID.

Column (2) – profile width measured at 50 per cent of the maximum in the integrated spectrum of a detection, corrected for the instrumental broadening, in km s^{-1}.

Column (3) – profile width measured at 20 per cent of the maximum in the integrated spectrum of a detection, corrected for the instrumental broadening, in km s^{-1}.

Column (4) – integrated flux in Jy km s^{-1} measured by defining a mask around a detection.

Column (5) – integrated flux in Jy km s^{-1} measured by defining a box around a detection using the MIRIAD task MBSPECT.

Column (6) – integrated peak flux in mJy measured by defining a mask around a detection.

Column (7) – integrated peak flux in mJy measured by defining a box around a detection using the MIRIAD task MBSPECT.

Columns (8), (9) & (10) – major and minor axes and position angle, respectively, of an ellipse fitted to the H I distribution of a detection at a column density level of 1.25×10^{20} atoms cm^{-2}. For the objects with WSRT-CVn IDs 7, 10, 11, 12, 15, 19, 22, 25, 30, 31, 42, 43, 47 and 61, only the equivalent parameters of a two-dimensional Gaussian fitted to the H I map are presented. The values presented have been deconvolved with a beam for all objects for which measurements have been carried out, with the exception of objects with the WSRT-CVn IDs 7 and 47 (we mark them with a '$\sim$' sign). Major and minor axes have been given in arcsec, and position angles are given in degrees. For the objects with an estimated size comparable to or smaller than the beam size, we use a '$<$' sign to indicate that these sizes are probably just upper limits.

ACKNOWLEDGMENTS

KK acknowledges financial support by The Netherlands Organization for Scientific Research (NWO), under Grant No. 614.031.014.

We are grateful to Jacqueline van Gorkom, Edwin Valentijn and Marc Verheijen for helpful discussions and the latter also for critical reading of an advanced version of this manuscript. We thank the referee for providing constructive comments and help in improving the contents of this paper.

The Westerbork Synthesis Radio Telescope is operated by the ASTRON (Netherlands Foundation for Research in Astronomy) with support from NWO. This research has made use of the NED which is operated by the Jet Propulsion Laboratory, California Institute of Technology, under contract with the National Aeronautics and Space Administration. We acknowledge the usage of the HyperLeda data base (http://leda.univ-lyon1.fr).

REFERENCES

Abazajian K. N. et al., 2009, ApJS, 182, 543

Avila-Reese V., Colín P., Valenzuela O., D'Onghia E., Firmani C., 2001, ApJ, 559, 516

Table 3. Properties of the H I detected objects (Part I).

WSRT CVn ID	NED name	Morph	RA (J2000) (h m s)	Dec. (J2000) (d m s)	V_{LG} (km s^{-1})	$Beam_a$ (arcsec)	$Beam_b$ (arcsec)	$Beam_{pa}$ (deg)	H I status
1	NGC 4359	SBc	12 24 11.1	31 31 18	1221.6	59.4	26.7	0.4	1
2	UGC07698	IB	12 32 54.4	31 32 28	310.9	57.4	27.0	1.6	1
3	UGC07428	IB	12 22 2.5	32 5 43	1112.1	59.6	26.4	−0.1	1
4	NGC 4509	Sab	12 33 6.8	32 5 30	917.3	54.9	27.3	0.3	1
5	MCG +06-28-022	Sc	12 43 7.1	32 29 26	884.6	53.4	29.0	0.3	1
6	KDG178	–	12 40 10.0	32 39 32	756.4	53.4	29.0	−0.8	1
7	FGC1497	Sd	12 47 0.6	32 39 5	509.9	57.4	27.8	0.7	1
8	UGCA292	I	12 38 40.0	32 46 1	295.8	57.1	27.9	0.3	1
9	CG1042	–	12 41 47.1	32 51 25	683.1	57.1	27.9	0.3	1
10	MAPS-NGP O_267_0609178	–	12 20 25.8	33 14 32	1036.2	50.5	27.3	−10.1	0
11	KUG1230+334A	Sbc	12 32 35.9	33 13 23	799.2	69.7	24.6	−11.6	0
12	KUG1230+336	Scd	12 33 24.9	33 21 3	826.1	69.7	24.6	−11.6	1
13	MAPS-NGP O_268_1525572	–	12 36 49.4	33 36 48	518.2	53.4	27.5	−1.8	0
14	NGC 4395	Sm	12 25 48.9	33 32 48	301.9	46.1	30.0	0.0	1
15	MAPS-NGP O_267_0529325	I	12 22 52.7	33 49 43	561.7	54.1	31.8	−5.1	1
16	UGC07916	I	12 44 25.1	34 23 12	606.0	55.8	28.7	0.6	1
17	KUG1216+353	–	12 19 0.6	35 5 36	753.8	53.6	29.1	−8.2	0
18	UGC07427	I	12 21 55.0	35 3 4	722.1	53.6	29.1	−8.1	1
19	MAPS-NGP O_268_1082578	–	12 44 25.5	35 11 48	879.1	51.8	29.7	−4.6	0
20	NGC 4534	Sd	12 34 5.4	35 31 8	803.6	51.8	29.6	−4.0	1
21	UGC07605	IB	12 28 38.9	35 43 3	311.7	49.4	31.9	0.0	1
22	KUG1230+360	–	12 33 15.1	35 44 2	821.7	52.7	30.5	0.2	0
23	UGC07949	I	12 46 59.8	36 28 35	340.6	58.9	29.4	6.2	1
24	UGC07559	I	12 27 5.1	37 8 33	224.8	63.0	28.2	−12.2	1
25	SDSS J123226.18+365455.5	–	12 32 26.5	36 54 40	879.6	57.0	30.7	−4.5	0
26	UGC07599	Sm	12 28 28.5	37 14 1	284.1	54.6	31.2	−5.3	1
27	UGC07699	SBc	12 32 48.0	37 37 18	507.5	53.4	30.3	−4.4	1
28	KDG105	I	12 21 43.0	37 59 14	582.9	49.3	29.1	−1.6	1
29	BTS133	ImIII	12 24 7.5	37 59 35	652.2	48.3	29.5	−1.5	0
30	BTS142	dE2	12 33 6.6	38 7 4	719.2	45.9	30.4	−2.3	0
31	BTS146	dE4	12 40 2.1	38 0 2	462.5	45.2	30.8	1.8	0
32	KUG1218+387	–	12 20 54.9	38 25 49	583.1	46.9	33.0	19.2	0
33	IC3687	IAB	12 42 15.1	38 30 12	369.0	45.8	31.2	8.5	1
34	UGCA290	Impec	12 37 21.8	38 44 38	472.4	52.2	30.9	−1.0	1
35	UGC07719	Sd	12 34 0.6	39 1 10	698.2	52.0	30.9	−1.1	1
36	NGC 4369	Sa	12 24 36.2	39 22 59	1047.1	50.5	31.6	−1.5	1
37	MCG+07-26-024	Sc	12 33 53.0	39 37 39	677.7	50.6	30.0	0.3	0
38	UGC07678	SABc	12 32 0.4	39 49 55	702.7	45.0	30.1	0.1	1
39	UGC07774	Sc	12 36 22.5	40 0 19	552.9	47.5	29.0	−0.5	1
40	–	–	12 33 24.3	40 44 51	1032.9	49.1	28.2	2.3	0
41	UGC07751	I	12 35 11.7	41 3 39	638.0	46.4	31.5	0.3	1
42	–	–	12 43 56.7	41 27 34	437.7	45.6	31.8	−0.5	0
43	MAPS-NGP O_218_0298413	–	12 31 9.0	42 5 39	597.8	49.3	31.0	0.3	0
44	MCG+07-26-011	Sd	12 28 52.2	42 10 41	441.3	45.2	31.8	0.3	1
45	MCG+07-26-012	Sc	12 30 23.6	42 54 6	474.3	45.5	29.5	0.2	1
46	UGC07690	I	12 32 26.9	42 42 15	573.8	45.5	29.5	0.3	1
47	[KK98]133	I	12 19 32.8	43 23 11	599.3	49.1	31.8	−1.3	0
48	UGC07608	I	12 28 44.2	43 13 27	578.2	46.7	33.0	0.0	1
49	UGC07577	I	12 27 40.9	43 29 44	237.3	43.8	31.6	0.0	1
50	LEDA166142	I	12 43 57.3	43 39 43	337.6	43.0	31.7	−0.6	1
51	MAPS-NGP O_172_0310506	–	12 49 31.0	44 21 33	564.7	41.7	29.6	−7.4	0
52	UGC07320	Sd	12 17 28.5	44 48 41	586.2	44.1	31.8	−1.5	1
53	NGC 4460	S0-a	12 28 45.5	44 51 51	547.7	45.3	31.2	−1.5	1
54	UGC07827	I	12 39 38.9	44 49 14	604.4	45.3	31.2	−1.1	1
55	SDSS J124759.96+445851.4	–	12 48 0.0	44 59 0	1212.0	40.5	29.2	1.2	0
56	NGC 4242	Sd	12 17 30.2	45 37 10	567.0	41.0	31.9	−0.3	1
57	UGC07391	Sc	12 20 16.2	45 54 30	788.6	42.6	32.7	0.0	0
58	UGC07408	I	12 21 15.0	45 48 41	514.1	44.7	31.5	0.0	1
59	NGC 4389	SBbc	12 25 35.1	45 41 5	771.2	42.5	32.8	0.0	1
60	UGC07301	Scd	12 16 42.1	46 4 44	758.3	47.8	30.1	−5.0	1
61	–	–	12 20 43.4	46 12 33	473.2	44.8	29.8	−3.1	1

Table 3 – *continued*

WSRT CVn ID	NED name	Morph	RA (J2000) (h m s)	Dec. (J2000) (d m s)	V_{LG} (km s^{-1})	$Beam_a$ (arcsec)	$Beam_b$ (arcsec)	$Beam_{pa}$ (○)	H I status
62	NGC 4288	SBcd	12 20 38.1	46 17 30	586.7	44.8	29.8	−3.1	1
63	NGC 4656	SBm	12 43 57.7	32 10 5	624.7	61.9	28.6	−1.2	1
64	NGC 4631	SBcd	12 42 8.0	32 32 29	571.1	53.4	29.0	−0.7	1
65	NGC 4618	SBm	12 41 32.8	41 9 3	568.9	48.5	30.5	0.6	1
66	NGC 4625	SABm	12 41 52.7	41 16 26	639.2	46.3	31.6	0.3	1
67A	NGC 4490	SBcd	12 30 36.4	41 38 37	618.3	46.2	31.6	0.1	1
67B	NGC 4485	IB	12 30 31.2	41 42 0	512.5	46.2	31.6	0.1	1
68	NGC 4449	Sc	12 28 11.9	44 5 40	245.8	45.4	30.9	2.5	1
69	NGC 4244	I	12 17 29.6	37 48 26	256.5	55.2	29.8	−5.8	1

Barkana R., Loeb A., 1999, ApJ, 523, 54
Barnes D. G. et al., 2001, MNRAS, 322, 486
Basilakos S., Plionis M., Kovač K., Voglis N., 2007, MNRAS, 378, 301
Beaulieu S. F., Freeman K. C., Carignan C., Lockman F. J., Jerjen H., 2006, AJ, 131, 325
Belokurov V. et al., 2008, ApJ, 686, L83
Blanton M. R. et al., 2003, ApJ, 592, 819
Blitz L., Spergel D. N., Teuben P. J., Hartmann D., Burton W. B., 1999, ApJ, 514, 818
Bode P., Ostriker J. P., Turok N., 2001, ApJ, 556, 93
Bouchard A., Jerjen H., Da Costa G. S., Ott J., 2005, AJ, 130, 2058
Braun R., Burton W. B., 2000, A&A, 354, 853
Braun R., Thilker D., Walterbos R. A. M., 2003, A&A, 406, 829
Bregman J. N., 1980, ApJ, 236, 577
Bregman J. N., 1996, in Kunth D., Guiderdoni B., Heydari-Malayeri M., Thuan T. X., eds, The Interplay Between Massive Star Formation, the ISM and Galaxy Evolution. Editions Frontières, Gif-sur-Yvette, p. 211
Davies J. et al., 2004, MNRAS, 349, 922
de Blok W. J. G., McGaugh S. S., van der Hulst J. M., 1996, MNRAS, 283, 18
de Heij V., Braun R., Burton W. B., 2002, A&A, 392, 417
de Vaucouleurs G., de Vaucouleurs A., Corwin Jr H. G., Buta R. J., Paturel G., Fouque P., 1991, Third Reference Catalogue of Bright Galaxies. Vol. 1–3, XII. Springer-Verlag, Berlin
Disney M. J., 1976, Nat, 263, 573
Disney M., Phillipps S., 1987, Nat, 329, 203
Duc P.-A., Bournaud F., 2008, ApJ, 673, 787
Duc P.-A., Papaderos P., Balkowski C., Cayatte V., Thuan T. X., van Driel W., 1999, A&AS, 136, 539
Efstathiou G., 2000, MNRAS, 317, 697
Eke V. R., Navarro J. F., Steinmetz M., 2001, ApJ, 554, 114
Geha M., Blanton M. R., Masjedi M., West A. A., 2006, ApJ, 653, 240
Giovanelli R. et al., 2005, AJ, 130, 2598
Gnedin N. Y., Kravtsov A. V., 2006, ApJ, 645, 1054
Grcevich J., Putman M. E., 2009, ApJ, 696, 385
Haynes M. P., Giovanelli R., Kent B. R., 2007, ApJ, 665, L19
Henning P. A., 1992, ApJS, 78, 365
Hubble E. P., 1926, ApJ, 64, 321
Huchra J. P., Vogeley M. S., Geller M. J., 1999, VizieR Online Data Catalog, 212, 10287
Huchtmeier W. K., Karachentsev I. D., Karachentseva V. E., Ehle M., 2000, A&AS, 141, 469
Jenkins A., Frenk C. S., White S. D. M., Colberg J. M., Cole S., Evrard A. E., Couchman H. M. P., Yoshida N., 2001, MNRAS, 321, 372
Kamionkowski M., Liddle A. R., 2000, Phys. Rev. Lett., 84, 4525
Karachentsev I. D. et al., 2003, A&A, 398, 467
Kauffmann G., White S. D. M., Guiderdoni B., 1993, MNRAS, 264, 201
Kent B. R. et al., 2007, ApJ, 665, L15
Kerr F. J., Henning P. A., 1987, ApJ, 320, L99
Kerr F. J., Sullivan W. T. III, 1969, ApJ, 158, 115
Klypin A., Kravtsov A. V., Valenzuela O., Prada F., 1999, ApJ, 522, 82
Koribalski B. S. et al., 2004, AJ, 128, 16
Kovač K., 2007, PhD thesis, Rijksuniversiteit Groningen
Kraan-Korteweg R. C., van Driel W., Briggs F., Binggeli B., Mostefaoui T. I., 1999, A&AS, 135, 255
Kravtsov A. V., Gnedin O. Y., Klypin A. A., 2004, ApJ, 609, 482
Krumm N., Brosch N., 1984, AJ, 89, 1461
Lang R. H. et al., 2003, MNRAS, 342, 738
Larson R. B., 1974, MNRAS, 271, L676
Lo K. Y., Sargent W. L. W., 1979, ApJ, 227, 756
Lockman F. J., 2003, ApJ, 591, L33
Makarova L., Karachentsev I., Takalo L. O., Heinaemaeki P., Valtonen M., 1998, A&AS, 128, 459
Matthews L. D., van Driel W., 2000, A&AS, 143, 421
Meyer M. J. et al., 2004, MNRAS, 350, 1195
Minchin R. F. et al., 2003, MNRAS, 346, 787
Minchin R. et al., 2005, ApJ, 622, L21
Minchin R. et al., 2007, ApJ, 670, 1056
Moore B., Ghigna S., Governato F., Lake G., Quinn T., Stadel J., Tozzi P., 1999, ApJ, 524, L19
Oort J. H., 1966, Bull. Astron. Inst. Netherlands, 18, 421
Oort J. H., 1970, A&A, 7, 381
Paturel G., Theureau G., Bottinelli L., Gouguenheim L., Coudreau-Durand N., Hallet N., Petit C., 2003, A&A, 412, 57
Pisano D. J., Barnes D. G., Gibson B. K., Staveley-Smith L., Freeman K. C., Kilborn V. A., 2004, ApJ, 610, L17
Pisano D. J., Barnes D. G., Gibson B. K., Staveley-Smith L., Freeman K. C., Kilborn V. A., 2007, ApJ, 662, 959
Press W. H., Schechter P., 1974, ApJ, 187, 425
Putman M. E., Gibson B. K., 1999, Pub. Astron. Soc. Aust., 16, 70
Putman M. E. et al., 1998, Nat, 394, 752
Putman M. E., Staveley-Smith L., Freeman K. C., Gibson B. K., Barnes D. G., 2003, ApJ, 586, 170
Quinn T., Katz N., Efstathiou G., 1996, MNRAS, 278, L49
Rand R. J., van der Hulst J. M., 1993, AJ, 105, 2098
Rand R. J., van der Hulst J. M., 1994, AJ, 107, 392
Read J. I., Pontzen A. P., Viel M., 2006, MNRAS, 371, 885
Rosenberg J. L., Schneider S. E., 2000, ApJS, 130, 177
Ryan-Weber E. V., 2006, MNRAS, 367, 1251
Sancisi R., Fraternali F., Oosterloo T., van der Hulst T., 2008, A&AR, 15, 189
Sault R. J., Teuben P. J., Wright M. C. H., 1995, in Shaw R. A., Payne H. E., Hayes J. J. E., eds, ASP Conf. Ser. Vol. 77. Astronomical Data Analysis Software and Systems IV. A Retrospective View of MIRIAD. Astron. Soc. Pac., San Francisco, p. 433
Schombert J. M., Bothun G. D., Schneider S. E., McGaugh S. S., 1992, AJ, 103, 1107
Shapiro P. R., Field G. B., 1976, ApJ, 205, 762
Shostak G. S., 1977, A&A, 54, 919
Simon J. D., Blitz L., Cole A. A., Weinberg M. D., Cohen M., 2006, ApJ, 640, 270
Sorar E., 1994, PhD thesis, Pittsburgh University
Spergel D. N., Steinhardt P. J., 2000, Phys. Rev. Lett., 84, 3760
Sternberg A., McKee C. F., Wolfire M. G., 2002, ApJS, 143, 419

Table 4. Properties of the H I detected objects (part II).

WSRT CVn ID	W_{50} (km s^{-1})	W_{20} (km s^{-1})	$S_{\rm int,c}$ (Jy km s^{-1})	$S_{\rm int,MBSPECT}$ (Jy km s^{-1})	$S_{\rm peak,c}$ (mJy)	$S_{\rm peak,MBSPECT}$ (mJy)	a (arcsec)	b (arcsec)	pa ($\circ$)
1	182.1	198.3	19.75	19.24	120	116	163.2	33.8	−74.1
2	45.1	60.0	36.54	36.13	585	580	192.4	177.6	−26.8
3	53.1	68.9	10.03	9.22	144	129	94.6	78.8	50.6
4	49.0	74.5	5.46	6.21	81	89	<51.1	36.6	49.8
5	26.7	39.7	1.11	0.86	25	22	<21.9	<13.5	−7.6
6	48.1	71.5	4.32	4.21	65	67	71.3	<25.9	−0.3
7	73.0	85.2	1.43	1.13	17	14	∼65.1	∼48.1	∼44.5
8	25.4	38.1	14.36	15.01	342	346	81.2	64.2	83.0
9	27.1	41.3	1.27	1.49	35	33	<33.8	<9.5	−5.2
10	33.9	60.2	0.32	0.72	10	12	<35.8	<18.4	3.4
11	33.3	58.5	1.32	1.68	27	30	<67.3	33.0	20.1
12	32.4	51.3	2.36	2.85	53	55	74.8	<22.3	56.5
13	29.5	42.7	0.92	0.83	20	18	<15.5	<11.5	−15.6
14	98.3	117.1	290.69	266.43	2679	2589	674.7	492.1	−49.4
15	19.4	31.2	0.45	0.59	12	16	<38.5	<14.9	−70.7
16	49.6	65.6	23.57	20.73	352	312	174.6	61.4	−1.6
17	67.4	101.7	1.23	1.58	23	19	<23.6	<16.6	1.3
18	31.8	47.2	3.59	3.59	74	74	54.0	36.1	27.4
19	37.7	73.2	0.44	0.41	10	7	<32.6	<24.7	81.4
20	109.8	124.3	67.58	66.17	570	564	247.3	159.0	−70.2
21	29.3	46.4	5.75	6.48	126	129	69.7	46.3	−15.1
22	37.2	96.1	0.66	1.36	16	20	<42.2	32.1	−43.7
23	24.2	33.9	17.52	15.31	412	381	132.9	103.8	37.3
24	49.5	67.0	27.06	26.11	401	388	196.1	80.8	−47.8
25	19.6	27.1	0.31	0.17	8	5	<46.4	<24.2	−13.4
26	54.2	73.1	11.86	12.11	171	168	127.5	54.2	−52.6
27	171.1	193.9	30.07	27.49	190	183	189.5	51.7	32.0
28	31.6	46.0	1.79	1.75	35	35	<38.4	<25.1	−73.3
29	28.8	52.8	1.69	2.38	41	41	<30.4	<25.9	−17.0
30	35.6	67.9	0.41	0.62	12	11	<45.9	<4.1	21.9
31	26.7	41.9	0.55	0.62	14	14	53.5	<16.0	−57.3
32	29.7	47.3	3.51	4.00	77	79	50.6	39.8	24.5
33	35.8	55.8	21.15	18.62	380	339	171.1	112.8	−15.1
34	32.5	62.2	1.46	1.80	32	32	<51.8	<8.9	58.0
35	57.3	78.6	11.29	10.83	149	145	106.9	33.2	−19.4
36	64.0	109.5	3.68	5.17	53	58	<40.6	39.8	24.1
37	32.5	51.3	5.35	5.94	108	113	70.6	45.7	8.3
38	39.3	60.5	5.93	7.08	107	121	64.9	43.9	65.5
39	182.7	204.6	25.46	25.88	147	141	201.9	36.5	−80.8
40	55.1	75.4	1.06	1.42	20	20	<24.3	<20.4	17.9
41	29.7	43.3	2.21	2.14	48	44	62.7	<18.8	4.8
42	18.7	28.4	0.38	0.72	18	21	52.0	<11.8	48.9
43	15.6	23.6	0.21	0.14	7	9	<32.4	<17.0	−19.4
44	53.5	76.1	3.46	3.45	52	47	53.9	<28.0	−18.1
45	36.1	52.9	2.30	2.78	46	51	52.3	<19.3	−62.9
46	71.0	88.0	21.49	21.45	246	243	135.2	87.9	30.9
47	50.7	59.4	0.47	0.63	11	10	∼60.7	∼36.8	∼28.4
48	43.3	61.3	28.45	26.64	456	438	176.1	168.7	−8.2
49	27.7	39.1	22.04	23.68	505	523	173.9	121.0	−53.6
50	21.8	31.1	0.75	0.76	21	20	<29.7	<7.0	5.9
51	35.8	71.1	0.84	1.25	20	21	<23.5	<3.2	36.1
52	55.2	74.4	1.49	1.64	22	23	<33.5	<20.3	51.5
53	89.7	128.3	3.51	4.30	33	41	50.5	<21.4	38.1
54	32.7	48.9	6.80	7.50	141	146	86.3	42.4	−37.8
55	49.6	65.8	2.01	1.98	31	30	42.6	<26.0	−16.3
56	108.0	125.2	31.00	26.70	270	223	247.0	155.7	30.9
57	58.0	74.5	2.27	2.50	34	34	46.3	<12.2	−6.5
58	24.9	39.6	3.69	4.78	92	107	61.1	47.0	9.0
59	146.2	159.8	6.11	5.06	41	34	88.4	45.7	−71.3
60	121.1	137.1	5.25	4.46	39	36	112.3	< 8.2	82.0
61	20.2	30.0	0.28	0.85	15	23	61.0	41.6	−17.3

Table 4 – *continued*

WSRT CVn ID	W_{50} (km s^{-1})	W_{20} (km s^{-1})	$S_{\rm int,c}$ (Jy km s^{-1})	$S_{\rm int,MBSPECT}$ (Jy km s^{-1})	$S_{\rm peak,c}$ (mJy)	$S_{\rm peak,MBSPECT}$ (mJy)	a (arcsec)	b (arcsec)	pa ($\circ$)
62	154.3	181.9	34.27	30.27	240	211	179.5	112.1	−49.3
63	146.2	174.7	–	299.98	–	2015	–	–	–
64	183.3	300.9	–	498.66	–	2711	–	–	–
65	90.2	114.9	–	59.80	–	580	–	–	–
66	50.7	70.3	–	38.43	–	569	–	–	–
67A	173.0	236.0	222.84	222.84	–	–	–	–	–
67B	139.0	168.0	29.11	29.11	–	–	–	–	–
68	97.5	138.3	–	238.97	–	2173	–	–	–
69	169.8	189.4	400.49	311.45	2386	1863	933.9	87.0	48.1

Taylor E. N., Webster R. L., 2005, ApJ, 634, 1067
Thom C., Putman M. E., Gibson B. K., Christlieb N., Flynn C., Beers T. C., Wilhelm R., Lee Y. S., 2006, ApJ, 638, L97
Thom C., Peek J. E. G., Putman M. E., Heiles C., Peek K. M. G., Wilhelm R., 2008, ApJ, 684, 364
Tully R. B., Fisher J. R., 1987, Nearby Galaxies Atlas. Cambridge Univ. Press, Cambridge
Valentijn E. A., 1994, MNRAS, 266, 614
Verde L., Oh S. P., Jimenez R., 2002, MNRAS, 336, 541
Verheijen M. A. W., Sancisi R., 2001, A&A, 370, 765
Verschuur G. L., 1969, ApJ, 156, 771
Wakker B. P., van Woerden H., 1991, A&A, 250, 509
Wakker B., Howk C., Schwarz U., van Woerden H., Beers T., Wilhelm R., Kalberla P., Danly L., 1996, ApJ, 473, 834
Wakker B., van Woerden H., de Boer K. S., Kalberla P., 1998, ApJ, 493, 762
Wakker B. P. et al., 2007, ApJ, 670, L113
Wakker B. P., York D. G., Wilhelm R., Barentine J. C., Richter P., Beers T. C., Ivezić Ž., Howk J. C., 2008, ApJ, 672, 298
Wall J. V., Jenkins C. R., 2003, Practical Statistics for Astronomers. Cambridge Univ. Press, Cambridge
West A. A., 2005, PhD thesis, University of Washington
Westmeier T., Brüns C., Kerp J., 2005, in Braun R., ed., ASP Conf. Ser. Vol. 331. Extra-Planar Gas Compact High-Velocity Clouds around the Galaxy and M31. Astron. Soc. Pac., San Francisco, p. 105
White S. D. M., Rees M. J., 1978, MNRAS, 183, 341
Wilcots E. M., Lehman C., Miller B., 1996, AJ, 111, 1575
Willman B. et al., 2005, ApJ, 626, L85
Wong O. I. et al., 2006, MNRAS, 371, 1855
Wu W., Keel W. C., 1998, AJ, 116, 1513
Yahil A., Tammann G. A., Sandage A., 1977, ApJ, 217, 903
York D. G. et al., 2000, AJ, 120, 1579
Zentner A. R., Bullock J. S., 2002, Phys. Rev. D, 66, 043003
Zucker D. B. et al., 2006, ApJ, 650, L41
Zwaan M. A., 2000, PhD thesis, Rijksuniversiteit Groningen, p. 152
Zwaan M. A., Briggs F. H., Sprayberry D., Sorar E., 1997, ApJ, 490, 173
Zwaan M. A. et al., 2004, MNRAS, 350, 1210
Zwaan M. A., Meyer M. J., Staveley-Smith L., Webster R. L., 2005a, MNRAS, 359, L30
Zwaan M., Meyer M., Webster R., Staveley-Smith L., The Hipass Team, 2005b, in Colless M., Staveley-Smith L., Stathakis R. A., eds, Proc. IAU Symp. 216, Maps of the Cosmos. Astron. Soc. Pac., San Francisco, p. 196

APPENDIX A: ATLAS OF H I OBSERVATIONS

Here, we present the H I images of the WSRT CVn detections overlaid over the DSS *B*-band images, their global H I profiles and position–velocity (PV) diagrams. A sample is presented here; the full appendix is available as Supporting Information in the online version of the article.

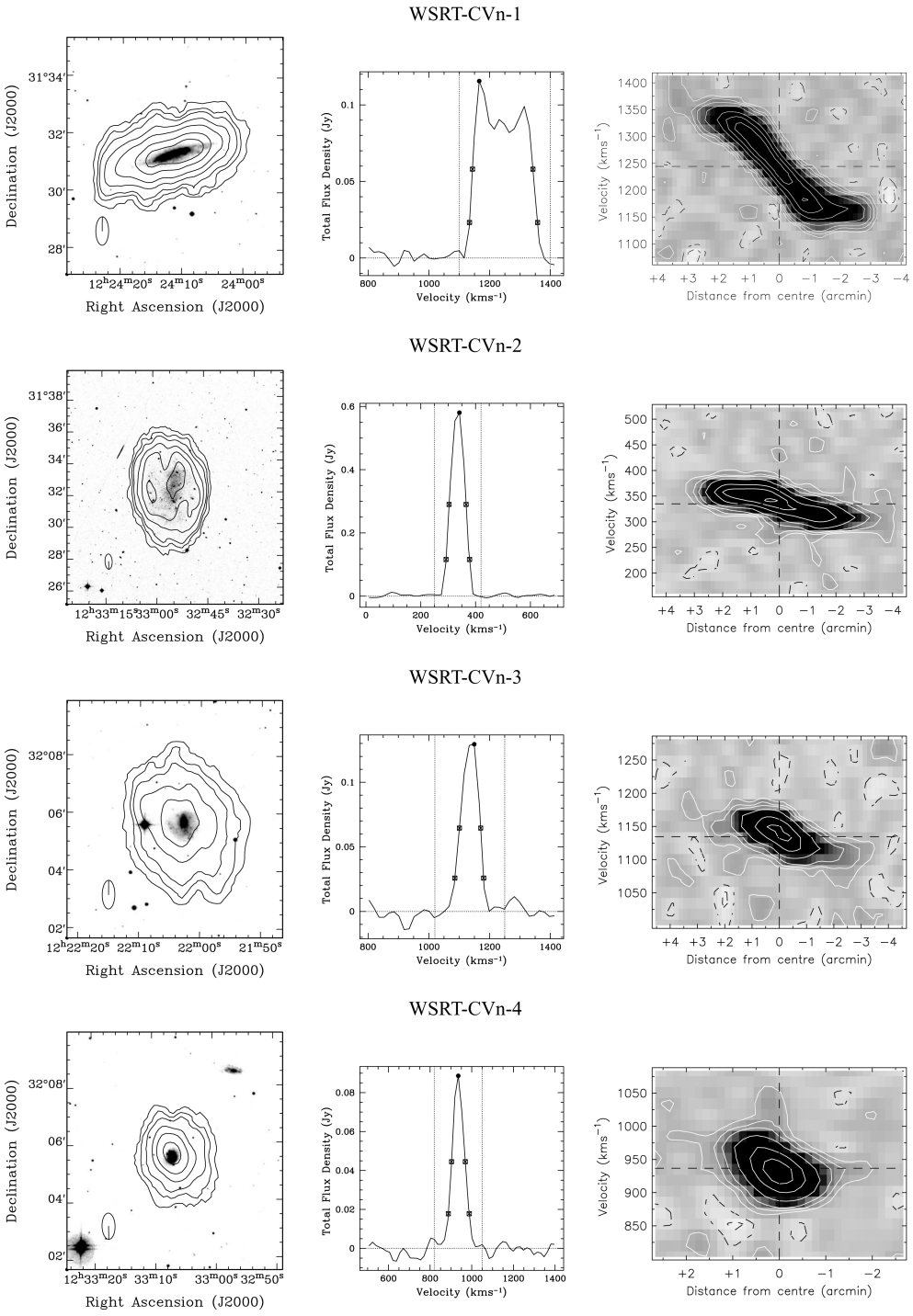

SUPPORTING INFORMATION

Additional Supporting Information may be found in the online version of this article.

Appendix A. Atlas of H I observations.

Please note: Wiley-Blackwell are not responsible for the content or functionality of any supporting information supplied by the authors. Any queries (other than missing material) should be directed to the corresponding author for the article.

This paper has been typeset from a TEX/LATEX file prepared by the author.